SYNCHROTRON RADIATION INTERFEROMETRY AT CEBAF

by

Sankalp Rajendra Shinde
B.S. May 2023, Fergusson College, India

A Thesis Submitted to the Faculty of
Old Dominion University in Partial Fulfillment of the
Requirements for the Degree of

MASTER OF SCIENCE

PHYSICS

OLD DOMINION UNIVERSITY
May 2025

Approved by:

Todd J. Satogata (Director)

Balša Terzić (Member)

Alexander Godunov (Member)

ABSTRACT

SYNCHROTRON RADIATION INTERFEROMETRY AT CEBAF

Sankalp Rajendra Shinde
Old Dominion University, 2025
Director: Dr. Todd J. Satogata

Synchrotron radiation interferometry is a method to measure transverse beam size in electron accelerators. By using synchrotron radiation interferometry at a dispersive location in CEBAF at Jefferson Lab, we measure the electron beam size and energy spread. This interferometry technique allows us to monitor the energy spread non-invasively, to measure precise electron beam rms energy spread for hypernuclear experiments, and verify that they meet experiment requirements in real time. This dissertation discusses the design, simulations, construction, and commissioning of this Synchrotron Radiation Interferometer (SRI) in the Hall C line at Jefferson Lab in 2024–2025.

This thesis is dedicated to the proposition
that the harder you work, the luckier you get.

ACKNOWLEDGMENTS

There are many people who have contributed to the successful completion of this dissertation. I extend many, many thanks to my committee members for their patience and hours of guidance on my research and editing of this manuscript. Special acknowledgment to Todd Satogata, Joe Gubeli, and Kevin Jordan who guided me during this project. Special gratitude to my academic advisor Dr. Balša Terzić who guided me through my Master's degree journey.

NOMENCLATURE

IHA	Instrumentation (harp profile monitor)
IHA3C05	Diagnostic harp in Hall C line (3C) downstream of MQK3C04
ILM	Instrumentation (beam loss monitor)
IPM	Instrumentation (beam position monitor)
ISR	Instrumentation (synchrotron radiation monitor)
MJA	Magnet (JA style dipole)
MJA3C08	JA-style dipole in Hall C (3C) line at location 08
MQK	Magnet (QK style quadrupole)
MQK3C04	K-style quadrupole in Hall C (3C) line at location 04
VIP	Vacuum (ion pump)
VRV	Vacuum (roughing valve)

TABLE OF CONTENTS

Page

LIST OF TABLES

LIST OF FIGURES

Figure Page

CHAPTER 1

INTRODUCTION

Hypernuclear experiments at Jefferson Lab investigate hypernuclei, or nuclei that contain one or more hyperons. In these experiments, hypernuclei are produced through collisions between the polarized CEBAF electron beam and fixed targets. Their primary goal is to analyze and identify hypernuclear states via high-resolution missing mass spectroscopy. Since the energy spread of the electron beam directly influences the precision of the missing mass reconstruction, maintaining a minimal energy spread is critical. A large energy spread broadens the spectral peaks, thereby reducing the resolution and complicating the identification of individual hypernuclear states [2].

To ensure that the anticipated hypernuclear energy states can be resolved, the beam's relative root-mean-square (RMS) energy spread must satisfy

$$\frac{\sigma_E}{E} < 3 \times 10^{-5} \,. \tag{1}$$

This constraint is very close to the CEBAF design energy spread at the energies of typical hypernuclear experiments, so there is little margin for additional energy spread due to machine drift or tuning errors. This CEBAF beam energy spread constraint at the experiment must therefore be continuously monitored to maintain an energy resolution sufficient for precise hypernuclear spectroscopy [3].

Synchrotron radiation interferometry offers a non-invasive method to measure the transverse beam size and energy spread in electron accelerators. By applying this technique at a dispersive location in the experiment hall, we will accurately measure the electron beam size and derive its corresponding energy spread in real time. This is essential for confirming that the beam parameters meet the stringent requirements of hypernuclear experiments.

This dissertation details the design, simulation, construction, and commissioning of the Synchrotron Radiation Interferometer (SRI) device installed in the Hall C transport line at Jefferson Lab during 2024–2025. It further explains the underlying beam measurements and the physics calculations required to extract the RMS energy spread from the SRI beam size measurements.

1.1 CONTINUOUS ELECTRON BEAM ACCELERATOR FACILITY (CEBAF)

The Continuous Electron Beam Accelerator Facility (CEBAF) is located at the Thomas Jefferson National Accelerator Facility (Jefferson Lab) in Newport News, Virginia. CEBAF is a continuous-wave electron beam accelerator which provides high-energy, polarized electron beams for nuclear physics experiments in four experimental halls (A, B, C, and D), as illustrated in Fig. 1. CEBAF accelerates electrons up to 12 GeV, and beam currents range from 1 μA to 100 μA in Hall C [4].

CEBAF's innovative recirculating beam transport system passes the electron beam through two linear accelerators (linacs) — the North and South linacs — multiple times using magnetic arcs. After each pass through a linac, the beam is redirected by bending magnets to the next pass through the opposite linac. There are ten recirculating arcs (ARC 1 through ARC 10), each corresponding to a different beam energy attained after successive passes; the last pass, which occurs in the North linac, achieves the highest energy of 12 GeV delivered to Hall D.

The acceleration process utilizes 1497 MHz Superconducting Radiofrequency (SRF) cavities in both linacs. CEBAF operates with recirculation passes labeled 1 through 5 (Fig. 1), and electron beams can be extracted from passes 1 to 5 for delivery to experimental halls A, B, and C, illustrated in the lower left corner of Fig. 1. CEBAF electron bunch lengths are 300 fs, much smaller than the 1497 MHz RF wavelength of 6.7×10^{-5} fs [4].

The SRI is installed along the Hall C transport line, identified in CEBAF element nomenclature as region 3C. It is specifically located near the dipole magnet MJA3C08 (see Fig. 2); the SRI utilizes synchrotron light emanating from bending of the electron beam in this dipole magnet.

Several relevant beam diagnostics are positioned in this area, including a harp for beam profile and emittance measurements (IHA3C12A), a vacuum ion pump (VIP3C12), a beam position monitor (IPM3C12), and a quadrupole magnet (MQK3C12). These diagnostics are used to characterize the beam emittance and Twiss parameters that are required to calculate the beam energy spread from SRI measurements.

This thesis is organized in several chapters. Chapter 2 gives the theory behind fundamental accelerator physics, synchrotron radiation, and how SRI measurements of beam size can be used to calculate momentum spread. Chapter 3 gives the experimental setup of the SRI in the Hall C line including optics transmission of optical elements. Chapter 4 gives the theory and background of beam emittance and Twiss parameter measurements with quadrupole scans, necessary inputs to calculating beam momentum spread. Chapter 5 describes full simulations of the experiment using the code Synchrotron Radiation Workshop to optimize the slit spacing and experiment configuration. Chapter 6 documents the SRI implementation, installation, and operations. Chapter 7 documents data acquisition and analysis results, before discussion in Chapter 8. Conclusions are provided in Chapter 9.

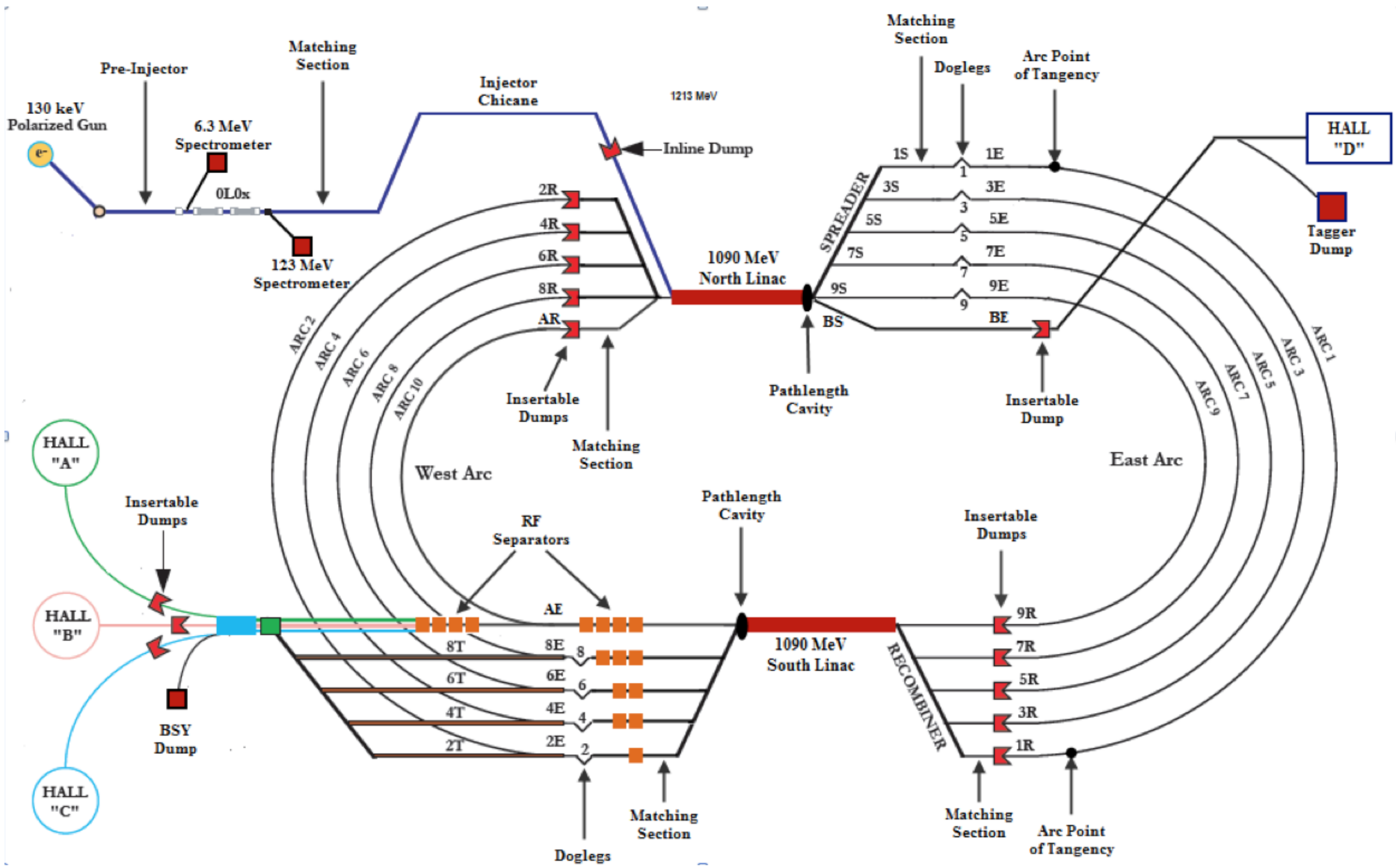

Figure 1. A schematic layout of CEBAF with electron beam energies are up to 12 GeV. North and South are the two linear accelerators.

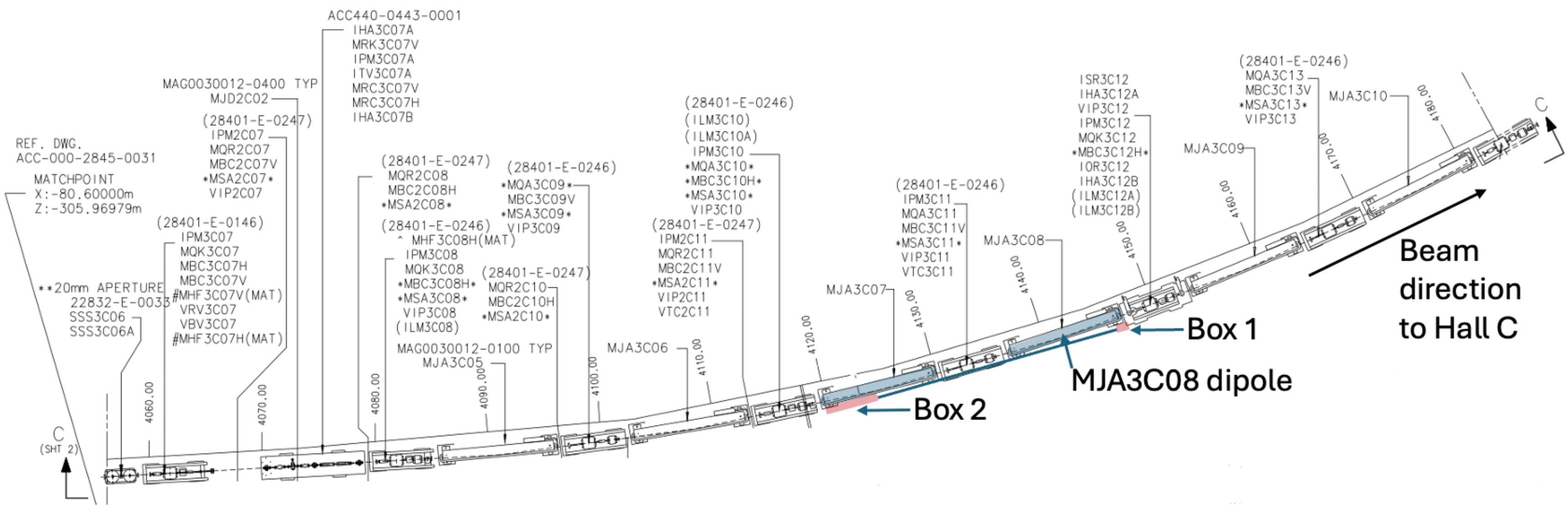

Figure 2. and Hall C SRI installation location downstream of dipole MJA3C08.

CHAPTER 2

THEORY

2.1 SYNCHROTRON RADIATION

When a charged particle such as an electron is bent along a curved trajectory within a magnetic field, it emits electromagnetic radiation known as synchrotron radiation. This emission results in an energy loss for the particle. As the electron follows its curved path, the radiation appears to originate from a segment of the arc with a length of roughly $\frac{2R}{\gamma}$, where R denotes the radius of curvature. Consequently, the observer only receives radiation during the brief period in which the electron is within that segment. The time interval, Δt, corresponding to the arc length is given by

$$\Delta t \approx \frac{R}{c\gamma^3}\,, \tag{2}$$

where c is the speed of light.

From this time interval, the critical frequency of the emitted radiation can be estimated as the inverse of Δt:

$$f_c \approx \frac{1}{\Delta t} \approx \frac{c\gamma^3}{R}\,. \tag{3}$$

More precisely,

$$f_c = \frac{3}{2}\frac{c\gamma^3}{R}\,. \tag{4}$$

In a bending magnet, the electron's trajectory is tangent to its instantaneous direction of motion. Moving at a relativistic speed along a path with constant curvature, the electron experiences acceleration in the radial direction, which in turn causes the emission of synchrotron radiation. In the electron's rest frame, the radiation is emitted symmetrically around the direction of acceleration according to

$$I(\theta') \propto \sin^2\theta', \tag{5}$$

where θ' is the emission angle in the electron's rest frame. No radiation is emitted along the acceleration direction in this frame which tells us $\theta' = 0$. When we consider the radiation pattern in the electron's lab frame, the radiation pattern is relativistically boosted instead of being emitted symmetrically. The emission angle in the lab frame θ is then related to the rest-frame emission angle θ' by

$$\tan\theta = \frac{\sin\theta'}{\gamma(1+\cos\theta')}. \tag{6}$$

For small angles, this relationship simplifies to

$$\theta \approx \frac{1}{\gamma}, \tag{7}$$

which means that the electron emits radiation in a narrow cone of angle approximately $1/\gamma$ around its direction of motion.

The electron emits this radiation over the arc of its trajectory; our detector selects a section of this emitted radiation code emitted along this small emission arc. This pulse has a length which depends on how long the electron remains within this small emission arc called the pulse length. As shown in Fig. 3, when the electron is at point A and point B the time difference between them

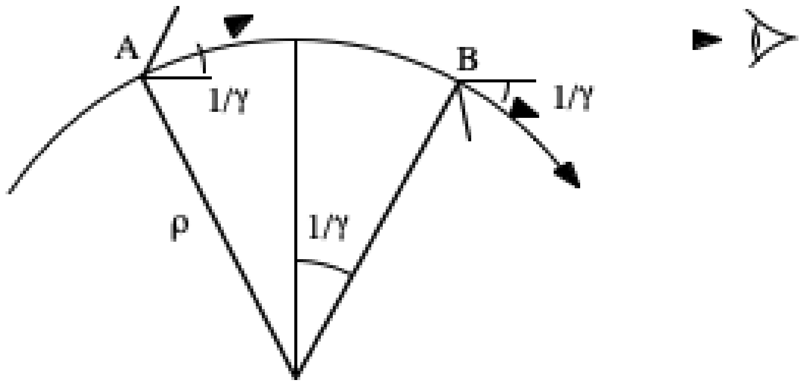

Figure 3. Radiation seen by an observer along arc of the trajectory. This radiation is emitted over a small arc of its trajectory [5].

determines the radiation pulse duration. The radiation pulse length is

$$\Delta t = t_B - t_A \approx \frac{\rho}{\gamma^3 c}\,. \tag{8}$$

The shorter the pulse duration, the broader the frequency spectrum. If we consider the time-frequency relation we have,

$$f \approx \frac{1}{\Delta t} \approx \gamma^3 \frac{c}{\rho}\,. \tag{9}$$

Higher electron energies γ lead to higher radiation frequencies. For CEBAF, radiation emitted is in the range of X-rays.

Figure 4 shows a relativistic electron bunch traveling through a bending magnet. The intensity of the emitted synchrotron radiation is proportional to the number of electrons in the beam:

$$I \propto N_{\text{electrons}}\,. \tag{10}$$

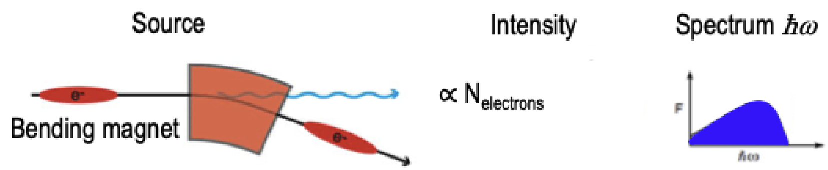

Figure 4. The intensity of radiation is proportional to the electron bunch intensity.

At higher currents the emitted synchrotron radiation becomes brighter in proportion to the current. The synchrotron radiation spectrum covers a wide range of photon energies, with a peak of the spectrum at the critical frequency f_c that depends on the electron energy and magnetic field [5].

2.2 BEAM DYNAMICS FOR THE SRI

2.2.1 Phase Space and Emittance

In accelerator physics, phase space is a multidimensional concept that represents the position and momentum coordinates of individual particles in a beam as they evolve in time t or, more typically, as the particles move in a distance coordinate s through the accelerator. Each particle occupies a unique point in this space, and the ensemble of these points defines the *phase space distribution* of the bunch. In the transverse planes, this distribution is often visualized as an ellipse whose shape and area are closely related to the beam's emittance.

The phase space coordinates used in this thesis are dependent on the time-like distance coordinate s:

- Horizontal: position $x(s)$ and angle $x'(s) = \frac{dx(s)}{ds}$
- Vertical: position $y(s)$ and angle $y'(s) = \frac{dy(s)}{ds}$

- Longitudinal: position $z(s)$ and momentum deviation $\delta(s) = \frac{p(s)-p_0}{p_0}$, where p_0 is the local design momentum

Emittance quantifies the extent of the phase space distribution and is a fundamental measure of beam quality. It reflects how tightly particles are confined both spatially and in angle. For a single bunch, the normalized root-mean-square (RMS) emittances are defined in each plane as ε_x, ε_y, and ε_p. In linear, conservative systems, emittance is conserved due to Liouville's theorem so it is not a function of s. It is also directly related to the beam's brightness.

2.2.2 Beta Function

The beta function $\beta(s)$ describes how the transverse RMS beam size evolves along the beamline coordinate s in a non-dispersive location. In the horizontal plane, the RMS beam size is given by:

$$\sigma_x(s) = \sqrt{\varepsilon_x \beta_x(s)}\,. \tag{11}$$

A similar expression holds for the vertical plane. Since emittance is constant in linear optics, variation in beam size along the accelerator is mostly attributed to changes in the beta function.

2.2.3 Beam Size Measurement

At a dispersive location, the total transverse beam size has two contributions, one from betatron motion as described above, and one from momentum spread:

$$\sigma_{\text{beam}}(s) = \sqrt{\varepsilon_x \beta_x(s) + \eta_x^2(s)\sigma_\delta^2(s)}\,, \tag{12}$$

where:

- $\eta_x(s)$ is the horizontal dispersion function (a property of the accelerator location), and
- $\sigma_\delta(s) \equiv \frac{\sigma_p(s)}{p_0}$ is the fractional momentum spread of the bunch in δ,

and similarly in the vertical plane. This expression highlights the dual contributions to the beam size: the intrinsic beam dynamics from the optics (via the beta function and emittance) and the energy spread effects amplified by dispersion. For clarity we omit explicit dependencies on accelerator location s and transverse x, y subscripts in further discussions.

For ultra-relativistic electrons such as those in CEBAF, the fractional momentum spread and fractional energy spread of the beam are equivalent. The fractional energy spread is then given by

$$\frac{\sigma_E}{E_0} = \sigma_\delta \quad \Rightarrow \quad \frac{\sigma_E}{E_0} \approx \frac{\sigma_{\text{beam}}}{\eta}, \tag{13}$$

where η is the dispersion at the measurement location and the approximation assumes the dispersion dominates the beam size, or $\varepsilon\beta \ll \eta^2\sigma_\delta^2$.

2.3 YOUNG'S DOUBLE SLIT INTERFEROMETER

Figure 5 shows the conventional Young's double slit interferometer setup. In this setup, a light wavefront travels from a source through an aperture at distance s' separated by distance D. The size of the aperture determines how much the light passes through the lens. Light propagates through the lens to distances s'_1 and s'_2. This propagated light intersects a detection plane to make an interference pattern intensity distribution $I(r')$, where r' is the transverse location on the detection plane relative to the experiment center line.

The visibility of this interference pattern depends on the coherence of light. This coherence of light depends on relative phases of arriving wave fronts. Constructive or destructive interference determines the intensity distribution of the interference pattern. Where arriving wave fronts are perfectly coherent, the interference pattern intensity is bright. Where the light is incoherent and there is destructive interference, the interference pattern will dim. Higher coherence gives us higher visibility.

The fringe visibility V measures the contrast in the interference fringes. It is defined as as

$$V \equiv \frac{I_{\max} - I_{\min}}{I_{\max} + I_{\min}}, \tag{14}$$

where $I_{\max}$ is the maximum intensity and $I_{\min}$ is the minimum intensity. High coherence produces high visibility, and high incoherence produces low visibility [6].

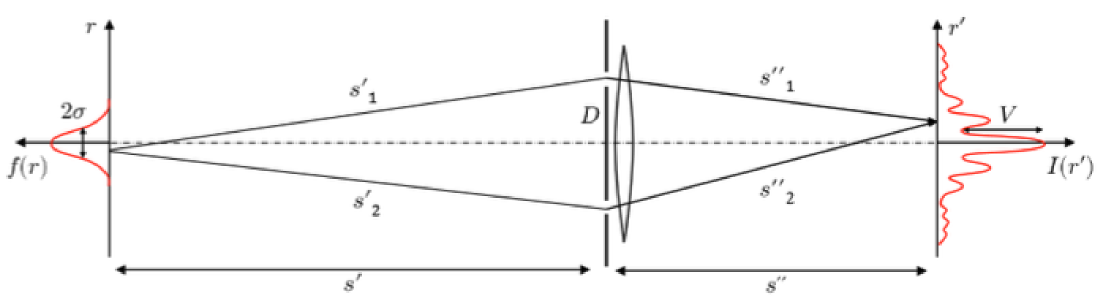

Figure 5. Young's double-slit interferometer: Interferometer is based on Young's double-slit experiment using a double slit setup.

If the incoming wavefronts from the two slits completely interfere constructively and destructively, we have $V = 1$ which produces high contrast fringes. If the light from the two slits is completely uncorrelated and the result is just the sum of two independent diffraction patterns, there is no interference pattern $V = 0$. The characteristics like fringe spacing and visibility of the interference pattern are directly related to the beam size and shape of the beam. The interference pattern is mathematically described as

$$I(x,y) = I_1(x,y) + I_2(x,y) + 2\sqrt{I_1(x,y)I_2(x,y)}\cos(\phi)\,, \tag{15}$$

where $I(x,y)$ is the intensity of the interference pattern at a given point (x,y). $I_1(x,y)$ and $I_2(x,y)$ are the intensities of the two interfering beams. ϕ is the phase difference between the two wavefronts.

2.4 SPATIAL COHERENCE

Spatial coherence is a property of waves that supports clear formation of an interference pattern. A wave is spatially coherent when the phase relationship between two points on the wavefront remains constant over a time. When spatial coherence is high, the wavefront maintains a well-defined phase structure over a large distance. This spatial coherence is described in terms of a mutual coherence function:

$$\Gamma(x_1,x_2) = \langle E^\star(x_1)E(x_2)\rangle\,, \tag{16}$$

where $E(x)$ is the electric field at position x and the star indicates the complex conjugate.

The degree of spatial coherence is described as

$$\mu(x_1,x_2) = \frac{\Gamma(x_1,x_2)}{\sqrt{I(x_1)I(x_2)}}\,, \tag{17}$$

where $I(x)$ is the intensity of the wave at position x. If $\mu(x_1,x_2) = 1$, the wave is fully coherent at these two points. If $\mu(x_1, x_2) = 0$, the wave is completely incoherent [7].

The visibility of fringes in the SLI is directly tied to the spatial coherence of the synchrotron radiation. High coherence will lead to V close to 1, while low coherence decreases V. Spatial coherence also refers to the angular distribution of the emitted radiation, which in turn depends on the size of the source. The transverse size of the electron beam determines the spatial extent of the radiation source. A smaller source size results in a broader angular distribution of radiation, which leads to higher spatial coherence. The spatial coherence of emitted synchrotron radiation helps us to calculate the transverse beam size using the Van Cittert-Zernike theorem.

2.5 VAN CITTERT-ZERNIKE THEOREM

If we consider a Fraunhofer diffraction region (wave fronts far from the source), we have a mutual coherence function of an optical field which is the Fourier transform of the intensity distribution of the source. Consider the mutual coherence function $\Gamma(x_1, x_2)$ between two observation points x_1 and x_2 in the far field

$$\Gamma(x_1, x_2) = \int I(S) e^{ikS(x_1 - x_2)} dS \,, \tag{18}$$

where $I(S)$ is the intensity distribution of the source, $k = \frac{2\pi}{\lambda}$ is the wave number of the emitted synchrotron radiation, S is the transverse coordinate on the source plane, and $x_1 - x_2 = D$ is the separation between the two observation points [7].

2.6 BEAM SIZE MEASUREMENT

To determine the transverse beam size using the interference pattern, we use the spatial coherence property and Van Cittert-Zernike theorem. Synchrotron radiation has a Gaussian intensity distribution in the transverse plane, since the source distribution of the electron beam is roughly Gaussian. This intensity distribution can be represented as

$$I(S) = I_0 e^{-S^2/2\sigma_x^2}\,, \tag{19}$$

where I_0 is the peak intensity at the center of the source, S is the transverse coordinate in the source plane, and σ_x is the standard deviation of the Gaussian profile. We use this intensity distribution as the source distribution and apply the Van Cittert-Zernike theorem. The mutual coherence function $\Gamma(D)$ is given by the Fourier transform of the source intensity distribution:

$$\Gamma(D) = \int_{-\infty}^{\infty} I(S) e^{ikSD} dS\,. \tag{20}$$

Substituting the Gaussian intensity profile:

$$\Gamma(D) = \int_{-\infty}^{\infty} I_0 e^{-S^2/2\sigma_y^2} e^{ikSD} dS\,. \tag{21}$$

This is a Gaussian Fourier transform,

$$\Gamma(D) = I_0 e^{-\frac{k^2 D^2 \sigma_y^2}{2}}\,. \tag{22}$$

We can see that the mutual coherence function decays exponentially as a function of the slit separation distance D. As was discussed in Section 2.4, spatial coherence determines the visibility of the interference pattern. The fringe visibility V was defined earlier as a measure of the contrast of the interference fringes:

$$V = \frac{I_{\max} - I_{\min}}{I_{\max} + I_{\min}}, \tag{23}$$

where $I_{\max}$ is the maximum intensity of the interference fringes, $I_{\min}$ is the minimum intensity. But the fringe visibility V is directly proportional to the magnitude of the mutual coherence function.

$$V(D) = \frac{|\Gamma(D)|}{I_0}, \tag{24}$$

where $\Gamma(D)$ is the mutual coherence function, and I_0 is the intensity of the source. So now we have a Gaussian intensity profile and we have coherence function as

$$\Gamma(D) = I_0 e^{-\frac{\pi^2 D^2 \sigma_y^2}{\lambda^2}}, \tag{25}$$

From the visibility-coherence relation,

$$V(D) = e^{-\frac{\pi^2 D^2 \sigma_x^2}{\lambda^2}}. \tag{26}$$

Rearranging to solve for beam size σ_x:

$$\sigma_x = \frac{\lambda}{\pi D}\sqrt{-\ln V}, \tag{27}$$

so by measuring fringe visibility at different slit separation D, we can extract the transverse beam size σ_x [6].

In our configuration at CEBAF, we have slits positioned at a distance SD from the source.

These represent the distance between the tangency point of the synchrotron light and the slits. We also have the slit gap (SG) defined as the distance between the two slits. The fringe separation is inversely proportional to the slit separation. If we take slit separation and slit gap into account, the equation for transverse beam size becomes

$$\sigma_x = \frac{\lambda SD}{\pi SG}\sqrt{0.5\ln\left(\frac{1}{V_x}\right)}, \tag{28}$$

where λ is the wavelength of synchrotron radiation, SD is the distance from beam tangency point to slits, SG is the slit gap, and V_x is the measured fringe visibility. In this case the slit separation SG is replaced by D, because the interference is created by two slits. The factor 0.5 comes from the assumption that the transverse profile of the electron beam is Gaussian. This reflects the reduction in fringe contrast due to the partial coherence of the beam, and ensures the correct scaling between the beam size and the observed visibility. It also ensures accurate conversion between the measured visibility and the transverse beam size for partially coherent light.

Once we obtain the measured beam size σ_{beam} and know the beam emittance ε_x and dispersion η_x from emittance and Twiss parameter measurements 4, we can infer the energy spread of the electron beam σ_δ at the SLI by inverting the equation for the beam size at a dispersive location:

$$\sigma_{\text{beam}} = \sqrt{\varepsilon_x\beta_x + \eta_x^2\sigma_\delta^2(s)} \quad \Rightarrow \quad \sigma_\delta = \frac{\sqrt{\sigma_{\text{beam}}^2 - \varepsilon_x\beta_x}}{\eta_x}. \tag{29}$$

Note that the sensitivity of determining the energy spread is best when the beam size is measured at a location where η_x is comparatively large, and β_x is comparatively small.

CHAPTER 3

EXPERIMENTAL SETUP

3.1 LOCATION AND OPTICS

The experimental setup for the SRI starts with identifying the location of the dipole generating the synchrotron light. Figure 6 shows the design Twiss parameters and dispersion for the Hall C line. The SLI was installed at CEBAF Accelerator MJA3C08 Dipole ($s = 77.3$m) in the Hall C line, as it has a modest $\beta_x = 15-23$m and the largest magnitude of dispersion ($\eta_x = -3.7$m) of any dipole in the line.

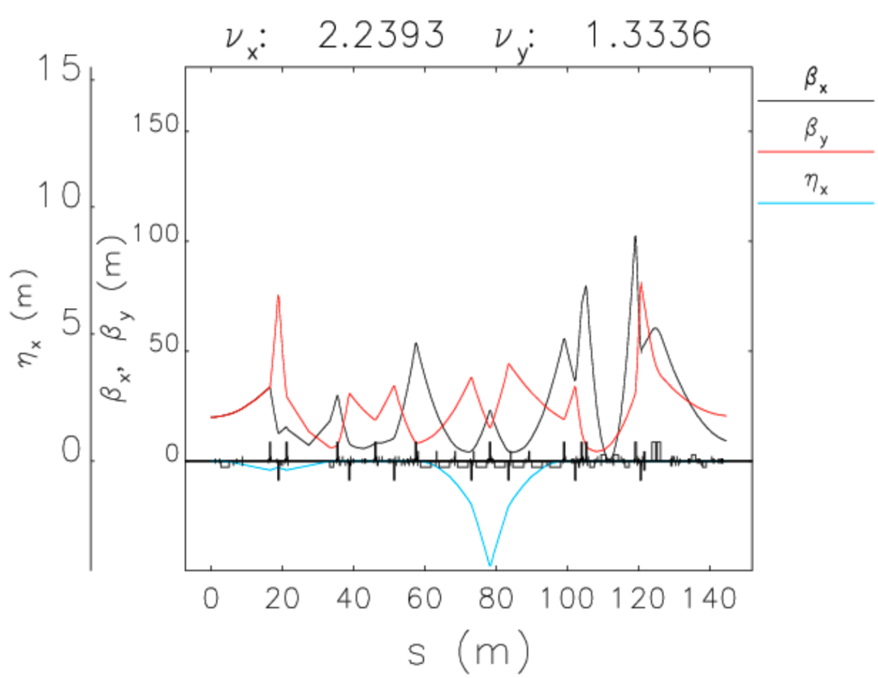

Figure 6. Twiss parameters of Hall C transport; the MJA3C08 dipole is located at $s = 77.3$m.

Figure 7 shows the plot which compares RMS beam size with and without dispersion or energy spread. In this plot, we have Beam energy in GeV on x-axis and Horizontal RMS beam size at MJA3C08 which is in micrometers.

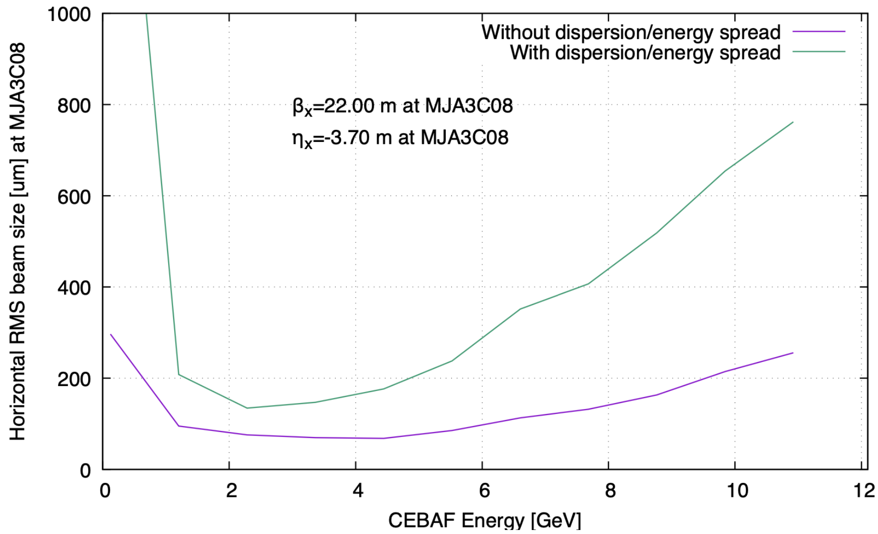

Figure 7. Horizontal RMS beam size at MJA3C08 as a function of the beam energy (GeV).

The purple line indicates the horizontal RMS beam size without dispersion and green line includes the additional effects due to dispersion and energy spread. Initially we see a decrease in beam size at lower energy as the energy is increased we see higher beam size without the contribution of dispersion. On the other hand, At very low energy with dispersion (Green line) shows very large beam size but reaches a minimum at around 2-3 GeV after this when beam energy is increased we can see significant increase in beam size since beyond 4 GeV, synchrotron radiation becomes significant which increases the energy spread and its squared contributes to the beam size to scale [8].

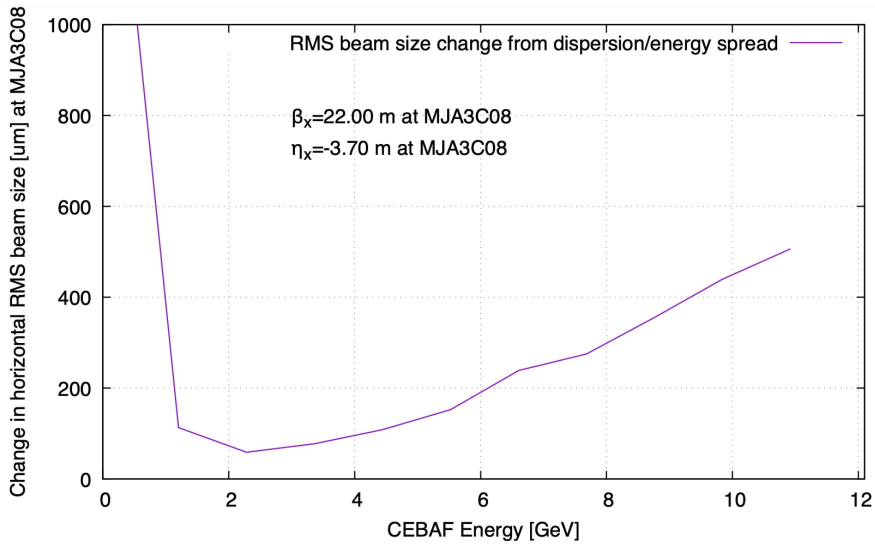

Figure 8. Change in horizontal RMS beam size at MJA3C08 due to the effects of dispersion and energy spread.

The difference of RMS beam sizes without and with the contribution of momentum spread and dispersion is shown in Fig. 8. At the lowest energy with the dispersion beam size is large since initially the electron beam has a large relative energy spread. This large relative energy spread, multiplied by dispersion ($\eta_x = -3.70$ m), creates a large initial beam size. The beam size decreases around 3 GeV, where the beam energy is high enough to significantly reduce relative energy spread but still not high enough for synchrotron radiation effects to dominate. From 4 GeV, beam size starts increasing since synchrotron radiation (SR) effects become prominent at higher energies. In short this two plots tells us that As the energy of electron beams increases, synchrotron radiation (SR) becomes a dominant which in turn affects emittance and energy spread. This tell us that by using Synchrotron Radiation Interferometer (SRI) technique, increase in synchrotron radiation intensity at higher energies can provide more accurate measurements of beam size and energy spread. Because energy spread has a more impact on the transverse beam size through dispersion. So at higher energies, SR interferometric method will detect small changes in energy deviation making very precise measurement of beam size and energy spread. In CEBAF, at higher passes we should see significantly less error in energy spread calculations [8].

3.2 EQUIPMENT LAYOUT

Figure 9 illustrates the complete layout of the experimental setup, which consist of a optical transport. This optical transport is arranged in a such a way that initially we have an insertable mirror (P-plane), a viewport, a turning mirror (P-Plane), and another turning mirror (S-plane). Box 1 is right after turning mirror (S-plane). In Box 1 we have only one turning mirror (S-plane). In box 1 is at the front end of the setup. At rear end of the setup we have another Box 2. In box 2 there is a polarizer, a bandpass filter, the lens, the slit stage and the camera. The layout of box 2 is shown in Fig. 10. The operating wavelength of the optical system is 450 nm.

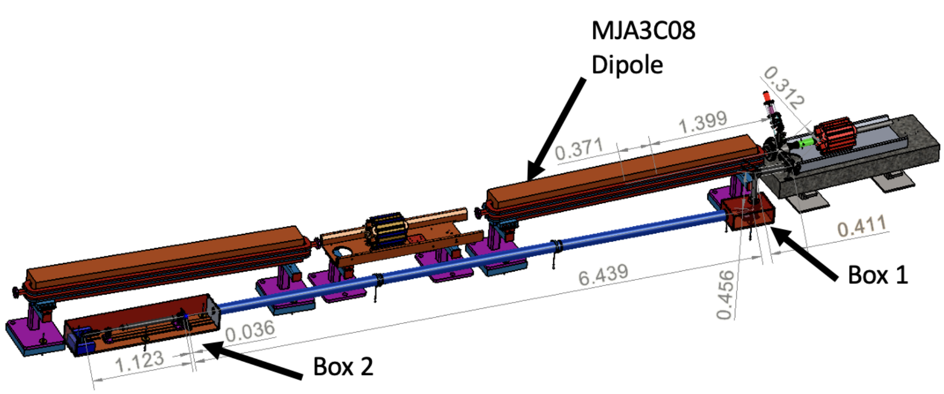

Figure 9. beam moves from left to right, showing dipoles MJA3C07 and MJA3C08. Synchrotron light is intercepted from the MJA3C08 dipole, and mirrored through box 1 (near the end of MJA3C08) before transport, optics, and detection in box 2 (adjacent to MJA3C07). Dimensions are in meters.

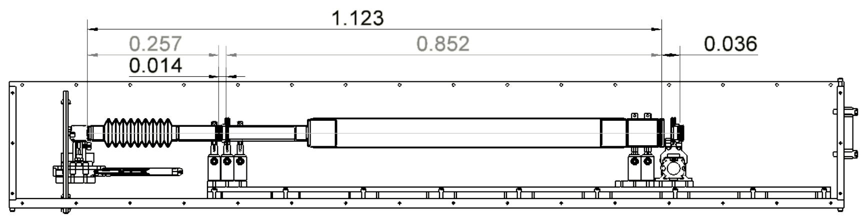

Figure 10. Box 2 contains the polarizer, bandpass filter, lens, slit stage and camera. Dimensions are in meters.

This optical transport setup is based on the classical optics thin lens equation. The thin lens equation relates the focal length of the lens to the distances of the object and the image from the lens. It is commonly stated as

$$\frac{1}{f} = \frac{1}{S_1} + \frac{1}{S_2}\,, \tag{30}$$

where f is the focal length of the lens, S_1 is the distance from the object to the lens, and S_2 is the distance from the image to the lens. In this case, the distance between the object which will be refer as a tangency point to the lens is S_1 = 9.424 m which is the combination of distance between tangency point to insertable mirror (1.399 m), insertable mirror to viewport (0.312 m), viewport to both turning mirrors(0.411 m + 0.456 m) and the distance between turning mirrors to lens (6.439 m + 0.036 m). The distance between image to lens is 1.123 m. Applying the thin lens equation:

$$\frac{1}{f} = \frac{1}{S_1} + \frac{1}{S_2} = \frac{1}{9.424\,\mathrm{m}} + \frac{1}{1.123\,\mathrm{m}} \quad \Rightarrow \quad f \approx 1\,\mathrm{m}\,. \tag{31}$$

Therefore the focal length of this lens is 1 m.

3.3 OPTICAL TRANSMISSION

To calculate the total throughput of this optical system, each optical element was selected on

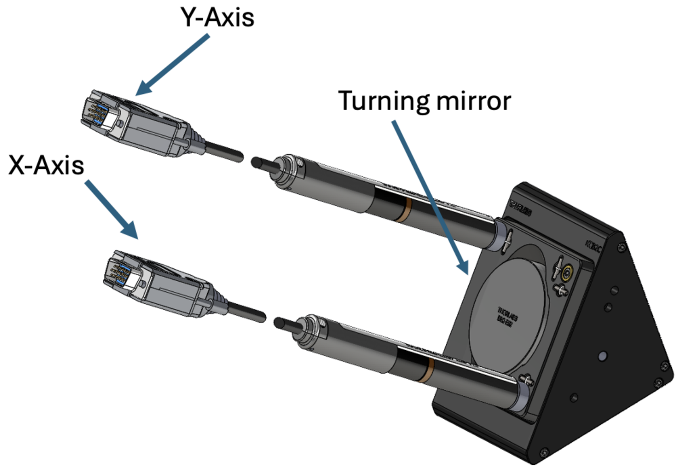

Figure 11. This turning mirror can be control in X and Y direction using DC motorTurning mirror with DC Servo Motor Actuators: This turning mirror can be control in X and Y direction using DC motor.

the basis of transmission and reflectivity data. This transmission and reflectivity data was seen at wavelength of 450 nm.

Insertable Mirror: The insertable aluminum substrate mirror is inserted into synchrotron beamline at a specific location. It can move in and out of the synchrotron beam's path. The main function of this mirror is to intercept the small part of synchrotron light beam emitted by charged particles through the dipole in the beamline. Figure 13 shows the transmission curve of this mirror. This figure shows the wavelength range from 400 nm to 700 nm at an average of 85% of reflectance at this range. We have about 90% reflectivity giving us highest reflectance at 450 nm.

Viewport: The viewport is the transparent window that allows synchrotron radiation to pass through. The main function of the viewport is to allow synchrotron radiation to pass from vacuum environment inside the accelerator to the our external experimental setup. The material that we are

Figure 12. Camera GigE Blackfly: Sony IMX226 sensor with 12 megapixels resolution with frame rate of 8.50 fps.

using in the viewport is quartz. The viewport is enhanced UV coated to allow maximum transport. Figure 14 shows the transmission curve of the viewport, made of quartz (fused silica), part number VPZL-275EU. We have 96% transmission of this viewport at 450 nm.

Turning Mirror P-Plane: The turning mirrors are dielectric mirrors that usually have high reflectivity. We have used one turning mirror for P-plane polarization and 2 mirrors for S-plane polarization. The turning mirror P-Plane is used to guide the radiation to other instruments in the setup. The P-Plane refers to parallel polarization. The plane of polarization of the Synchrotron light beam. The electric field vector of the light is parallel to the plane of incident. Figure 15 shows that at 450 nm we get 98.95% reflectance for the P-plane which is in blue color, and 100% reflectance for S-plane which is in red color. This ensures that selected 3-turning mirrors have highest reflectivity at 450 nm.

Turning Mirror S-Plane: The turning mirror S-Plane is used to also guide and change the direction of the synchrotron radiation light through the optical setup. S-plane refers to perpendicular polarization. When the electric field vector of light is perpendicular to plane of the incident. The reflectivity of the mirror BB2-E02 at 450 nm is 100%.

Polarizer: The polarizer is used to select the polarization of synchrotron radiation beam. Polarizers ensures that only light with a particular polarization component is transmitted. The total transmission for polarizer WP25M-VIS at 450 nm is 99.79%.

Bandpass Filter: The bandpass filter is an optical device that allows light within a specific range of wavelength to pass through, while blocking other wavelengths. A hard coated bandpass filter (FBH473-3) is used. This bandpass filter is designed for 450 nm wavelength. As we can see in Fig. 16 at 450 nm, we have highest transmission of 97.70%.

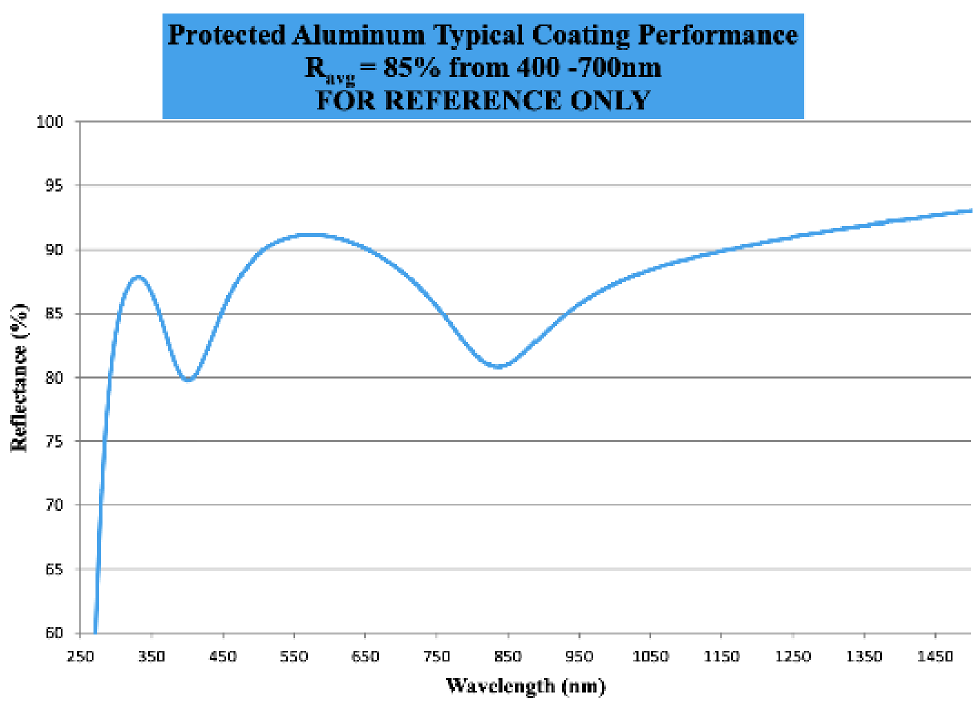

Figure 13. Reflectance vs Wavelength plot for Insertable mirror. Wavelength range from 400 nm to 700 nm at an average of 85%.

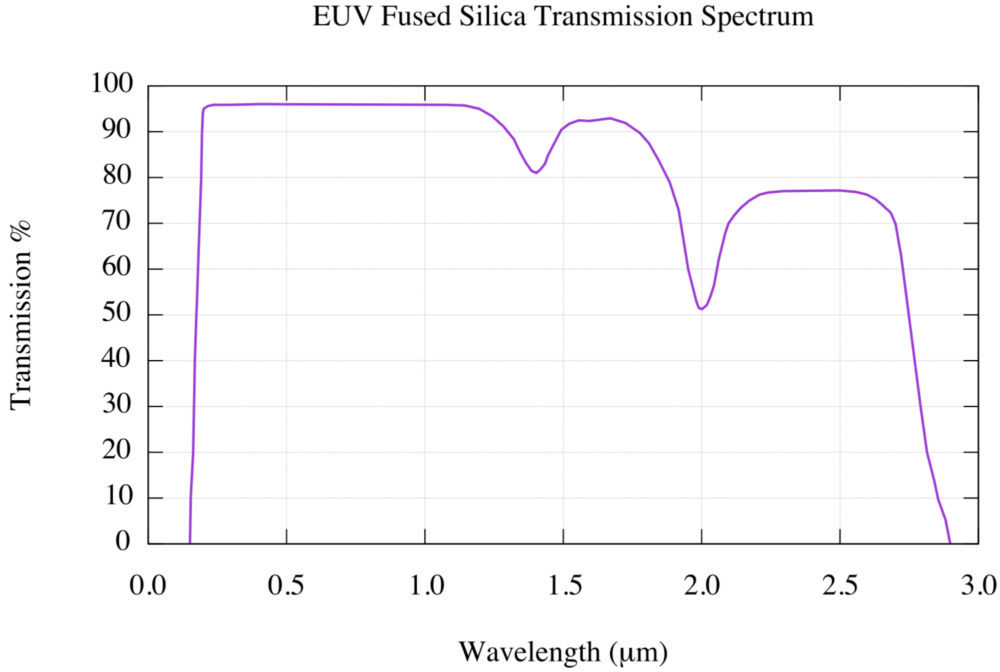

Figure 14. Transmission vs Wavelength for Viewport. 96% transmission at 450 nm. This has highest transmission at 450 nm.

As is shown in Table 1, we get total transmission of 50.45%. At first synchrotron light is intercepted by the insertable mirror. A small part of synchrotron light is capture which is emitted by charged particles through the dipole (MJA3C08). This light then passes through the viewport, which transfers synchrotron light from vacuum environment to the interferometer setup. Firstly synchrotron light appears on the two turning mirror P-Plane and then on two turning mirror S-Plane shown in Fig. 17. The main function of this turning mirror is guide or transfer the synchrotron light on to slits and camera screen. This turning mirrors are controlled by 12 mm Travel, DC Servo Motor Actuators. This Actuators controls the turning mirror in X and Y direction. In Fig. 11 we can see the two actuators are connected to the 3rd turning mirror. This actuators are controlled by DC Servo motor. Synchrotron light is aligned using the turning mirrors, it is then passed onto

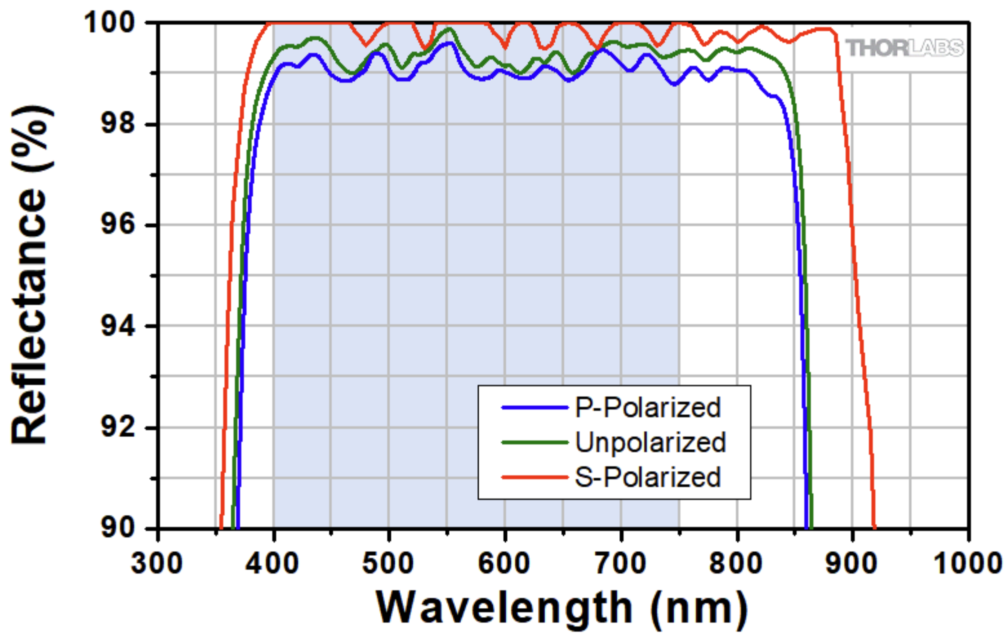

Figure 15. Reflectance vs Wavelength for 3 Turning mirrors. At 50 nm we get 98.95% reflectance for P-plane (blue color) and 100% reflectance for S-plane (red color) at 450 nm.

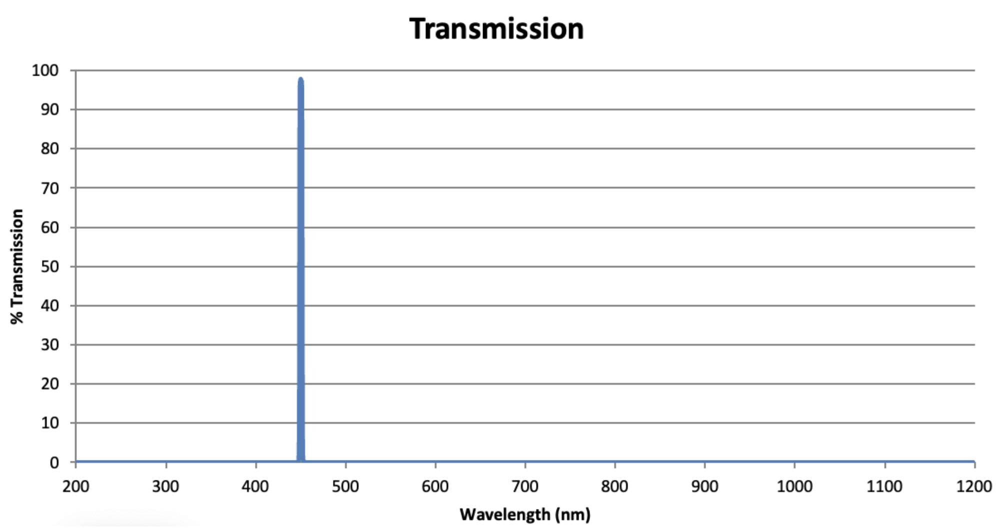

Figure 16. Transmission vs Wavelength for Bandpass filter: The highest transmission of 97.70% is at 450 nm.

the double slit followed by polarizer and bandpass filter. At the end, synchrotron light is passed through the lens and then onto the camera. The camera we are using is PoE GigE Blackfly which is a monochrome camera. It has a Sony IMX226 sensor with full 12 megapixels resolution with frame rate of 8.50 fps (frames per second). Other main feature of this camera is that it can be connected to any external hardware for extracting the image and further data acquisition. Initially this optical transport system was tested using the Laser point source for proper alignment. This was done to ensure the synchrotron light would properly align with all mirrors to transport the synchrotron light on to the lens and the camera.

Table 1. Synchrotron Light (λ=450 nm) Transmission Contributions by Item and Part Number.

Item	**PN**	**Transmission 450 nm**
Insertable mirror	47-113	85.00%
Viewport	VPZL-275EU	96.00%
Turning Mirror P-Plane	BB2-E02	98.95%
Turning Mirror S-Plane	BB2-E02	100.00%
Turning Mirror S-Plane	BB2-E02	100.00%
Polarizer	WP25M-VIS	85.45%
BandPass	FBH450-3	97.70%
Lens	LA1779-A	99.79%
Camera QE		75.00%
Total		**50.45%**

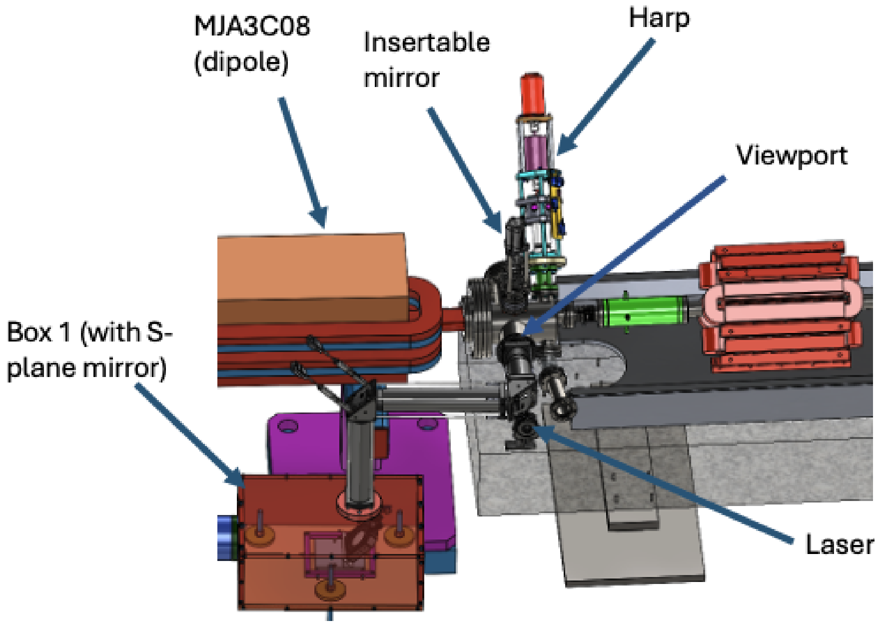

Figure 17. Initial optical transport: It shows the MJA3C08 dipole, Harp, Insertable mirror, Viewport, Laser and first box with S-plane mirror.

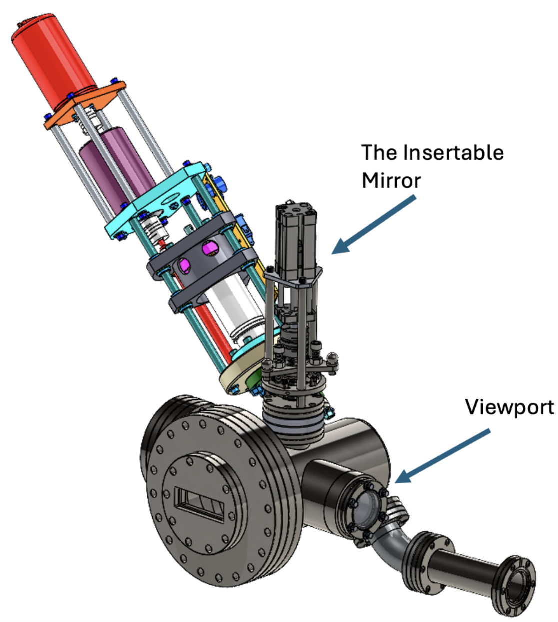

Figure 18. Insertable mirror and viewport: insertable mirror inserted into synchrotron beamline at a specific location and Viewport is connected after the mirror.

CHAPTER 4

TWISS PARAMETER AND EMITTANCE MEASUREMENTS

4.1 TWISS PARAMETERS

The Twiss parameters are used to describe the particle beam in phase space; they are also called Courant-Snyder parameters after the authors of a foundational work of strong focusing in accelerator physics [9]. These parameters describe the shape of the beam ellipse in transverse (horizontal, x, or vertical, y) phase space as a function of the longitudinal coordinate s. There are three main Twiss parameters that describe the beam ellipse in the phase space.

The beta functions $\beta_{x,y}(s)$ relate the beam emittances $\varepsilon_{x,y}$ and RMS beam sizes $\sigma_{x,y}(s)$:

$$\beta_{x,y}(s) = \frac{\sigma^2_{x,y}(s)}{\varepsilon_{x,y}}\,. \tag{32}$$

A larger beta function gives a larger beam size for the same beam emittance.

The alpha functions $\alpha_{x,y}(s)$ quantify the rate of change of the beta function in the beam direction s.

$$\alpha_{x,y}(s) = -\frac{1}{2}\frac{d\beta_{x,y}(s)}{ds}\,. \tag{33}$$

It also is visualized as the tilt of the phase space ellipse. The alpha function $\alpha_{x,y}(s)$ indicates whether the beam size $\sigma_{x,y}(s)$ is getting larger (negative alpha) or smaller (positive alpha) as the beam evolves in s.

The gamma functions $\gamma_{x,y}(s)$ quantify the angular spread, or divergence, of the beam:

$$\gamma(s) = \frac{1+\alpha(s)^2}{\beta(s)} \,. \tag{34}$$

The $\gamma(s)$ function is inversely proportional to $\beta(s)$ function. When β is large, γ becomes small so the beam becomes wide. When β is small, γ becomes large and beam is narrow. The gamma function describe how strongly the beam is focusing at given location in the accelerator.

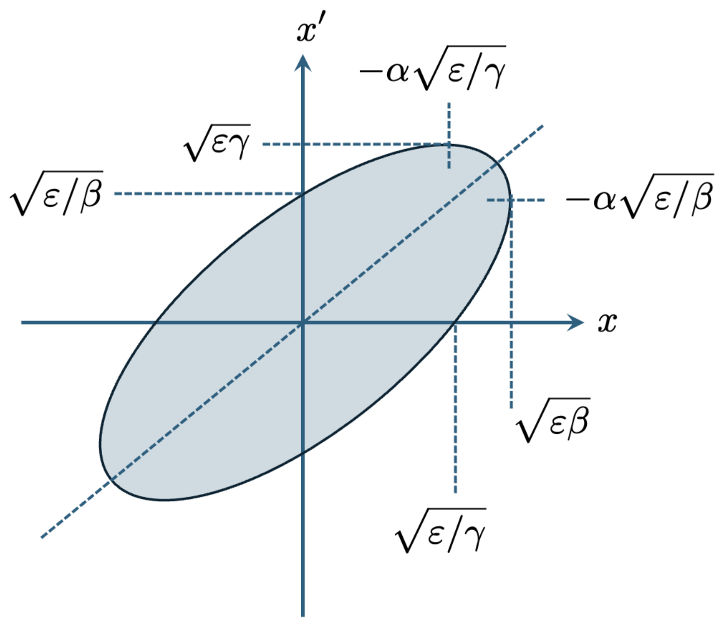

Figure 19. Courant-Snyder Ellipse: This describes the shape of the beam ellipse.

Figure 19 shows the Courant-Snyder phase-space ellipse. In this section we want to measure this Twiss parameters at the location of the interferometer where we measure beam size. The measurement of these twist parameters are critical for the beam size measurement using a synchronization radiation interferometer.

4.2 TRANSPORT MATRIX

The transport matrix M tells us how the particle's position and angle develop as it moves through various optical elements, such as drift spaces, quadrupoles and bending magnets. The transport matrix allows us to calculate the new position and angle of a particle in a beamline. This matrix is described as

$$\begin{pmatrix} x' \\ x' \end{pmatrix}_{\text{new}} = M \begin{pmatrix} x \\ x' \end{pmatrix}_{\text{old}} , \tag{35}$$

where x is a transverse position of the particle. x' is an slope of trajectory which is transverse angle. The determinant of this transport matrix is always one which means it does not affect the total size of the system. By multiplying the two matrices we can define the total effect of particle moving through two sections. The most common elements in an beamline are drift spaces, and focusing and defocusing quadrupoles. Each of these elements has their own transport matrix.

The transport matrix for a drift is

$$M_{\text{drift}} = \begin{pmatrix} 1 & L \\ 0 & 1 \end{pmatrix} . \tag{36}$$

This matrix describes the particles which travel freely over a distance L. Here it does not have any focusing element along the distance L.

The transport matrix for a focusing quadrupole is

$$M_{\text{fq}} = \begin{pmatrix} \cos(L\sqrt{K}) & \frac{1}{\sqrt{K}}\sin(L\sqrt{K}) \\ -\sqrt{K}\sin(L\sqrt{K}) & \cos(L\sqrt{K}) \end{pmatrix} . \tag{37}$$

As the name suggest quadrupole magnet focuses the beam where K is the strength of the quadrupole and L is the length. The sin and cosine terms suggests the trajectory due to focusing effect of the quadrupole.

The transport matrix for a defocusing quadrupole is

$$M_{\mathrm{dq}} = \begin{pmatrix} \cosh(L\sqrt{K}) & \frac{1}{\sqrt{K}}\sinh(L\sqrt{K}) \\ \sqrt{K}\sinh(L\sqrt{K}) & \cosh(L\sqrt{K}) \end{pmatrix}. \tag{38}$$

This quadrupole magnet defocuses the beam. The cosh and sinh terms suggest that the effect on the beam is wider which means beam is defocused instead of focusing.

Thin-lens approximation: The basic quadrupole magnet has a transport matrix Q which describes the position and strength K of the magnet.

$$Q = \begin{pmatrix} 1 & 0 \\ K & 1 \end{pmatrix}, \tag{39}$$

where $K = \frac{1}{f}$ is the strength of quadrupole of focal length f. In Thin lens approximation quadrupole magnet acts as lens. Lens focuses the light gradually long the distance which is mostly depends on the thickness of the lens. But if we ignore the thickness of the lens it focuses light all at once. So just like lens quadrupole magnet has some finite length where particles gradually change direction while passing through it. So by applying thin-lens approximation we assume that quadrupole length L is much smaller than its focal length f, or $L \ll f$.

4.3 QUADRUPOLE SCAN METHOD

The quadrupole scan method is used to measure transverse emittance in an accelerator. The goal of this method is to measure the beam size of the particle beam as a function of magnetic field strength of a quadrupole magnet. This measurement is taken using a wire scanner. By this method we can measure the beam size, Twiss parameters and beam emittance. Emittance is a measure of the spread of the particle beam in phase space which corresponds to position and momentum. It represents how particle beams are distributed in phase space mostly describing the size and divergence of particle beam. The particle distribution in transverse phase space can be described in a matrix form [10].

$$\Sigma_{\text{beam}} = \begin{bmatrix} \Sigma_{11} & \Sigma_{12} \\ \Sigma_{21} & \Sigma_{22} \end{bmatrix}, \tag{40}$$

where Σ_{11} is related to the square of the beam size $\langle x^2 \rangle$, Σ_{22} is related to the angular divergence $\langle x'^2 \rangle$ and Σ_{21} represents correlations between position and angle, q$\langle x\ x' \rangle$. With the help of this beam matrix we can also define the geometrical emittance of the beam as

$$\varepsilon = \pi\sqrt{\det(\Sigma_{\text{beam}})}, \tag{41}$$

where $\det(\Sigma_{\text{beam}})$ is the determinant of the beam matrix.

$$\det(\Sigma_{\text{beam}}) = \Sigma_{11}\Sigma_{22} - \Sigma_{12}\Sigma_{21}\,. \tag{42}$$

This geometrical emittance describes the area of the beam ellipse divided by π. Using this definition, we can expressed beam ellipse and matrix in terms of Courant-Snyder parameters as

$$\varepsilon = \gamma x^2 + 2\alpha x x' + \beta x'^2\,, \tag{43}$$

where $\gamma = \Sigma_{22}/\varepsilon$, $\alpha = -\Sigma_{12}/\varepsilon$, and $\beta = \Sigma_{11}/\varepsilon$. This is how beam matrix can be expressed in terms of Twiss parameters. $\Sigma_{11}, \Sigma_{12}, \Sigma_{22}$ can be characterize as statistical moments of the particle distribution in a phase space.

$$\Sigma_{11} = \langle x^2 \rangle\,. \tag{44}$$

This is described as the square of the beam size.

$$\Sigma_{12} = \Sigma_{21} = \langle x x' \rangle\,. \tag{45}$$

This is described as the correlation between position and angle

$$\Sigma_{22} = \langle x'^2 \rangle\,. \tag{46}$$

This is described as the square of the beam divergence. Therefore the root mean square (RMS) emittance can be describe as

$$\varepsilon_{rms} = \beta\gamma\sqrt{\langle x^2 \rangle \langle x'^2 \rangle - \langle x x' \rangle^2}\,. \tag{47}$$

To calculate emittance and Twiss parameters using the quad scan method, we consider conditions where the beam is traversing through a quadrupole with varying strength K, and the beam size

Σ_{harp} is measured at a downstream harp scanner as a function of this strength. The thin quadrupole transfer matrix for a focusing quadrupole is:

$$Q = \begin{pmatrix} 1 & 0 \\ -K & 1 \end{pmatrix}, \tag{48}$$

where $K = \frac{1}{f}$. The transport matrix from the end of this quadrupole to harp is parameterized as

$$M_{\text{q2h}} = \begin{pmatrix} M_{11} & M_{12} \\ M_{21} & M_{22} \end{pmatrix}. \tag{49}$$

The total transfer matrix from the start of the quadrupole to the harp is the product of these matrices:

$$M_{\text{tot}} = M_{\text{q2h}} Q, \tag{50}$$

$$M_{\text{tot}} = \begin{pmatrix} M_{11} - KM_{12} & M_{12} \\ M_{21} - KM_{22} & M_{22} \end{pmatrix}. \tag{51}$$

We then determine how the beam size is transformed by the quadrupole and measured at the harp:

$$\Sigma_{\text{harp}} = M_{\text{tot}} \Sigma_0 M_{\text{tot}}^T. \tag{52}$$

Expanding the (1,1) component of the matrix,

$$\Sigma_{11} = (M_{11} - KM_{12})^2 \Sigma_{110} + 2(M_{11} - KM_{12}) M_{12} \Sigma_{120} + M_{12}^2 \Sigma_{220}. \tag{53}$$

Further expanding terms:

$$\Sigma_{11} = M_{11}^2\Sigma_{110} - 2M_{11}M_{12}\Sigma_{110}K + M_{12}^2\Sigma_{110}K^2 \quad +2M_{11}M_{12}\Sigma_{120} - 2M_{12}^2\Sigma_{120}K + M_{12}^2\Sigma_{220}\,.$$

Rearranging the terms:

$$\begin{aligned}\Sigma_{11} =&(M_{11}^2\Sigma_{110} + 2M_{11}M_{12}\Sigma_{120} + M_{12}^2\Sigma_{220})\\ &-2(M_{11}M_{12}\Sigma_{110} + M_{12}^2\Sigma_{120})K\\ &+M_{12}^2\Sigma_{110}K^2\,.\end{aligned}$$

This is a quadratic equation in K which tells us how the beam size changes with the quadrupole strength. We can also rewrite this equation in the form of quadratic coefficients,

$$\Sigma_{11} = AK^2 + BK + C\,, \tag{54}$$

where:

$$\begin{aligned}A &\equiv M_{12}^2\Sigma_{110}\\ B &\equiv -2(M_{11}M_{12}\Sigma_{110} + M_{12}^2\Sigma_{120})\\ C &\equiv M_{11}^2\Sigma_{110} + 2M_{11}M_{12}\Sigma_{120} + M_{12}^2\Sigma_{220}\,.\end{aligned}$$

We obtain these coefficients by fitting the measured beam size to a quadratic function in K. Since we know that the determinant of the sigma matrix is the square of the beam emittance, we can infer

$$\varepsilon_0^2 = \det\Sigma = \frac{AC}{M_{12}^4} \quad \varepsilon_0 = \frac{\sqrt{AC}}{M_{12}^2}\,. \tag{55}$$

The Twiss parameters at the quadrupole can then be obtained by

$$\begin{aligned}
\beta_0 =& \frac{\Sigma_{11_0}}{\varepsilon_0} = \sqrt{\frac{A}{C}} \\
\alpha_0 =& -\frac{\Sigma_{12_0}}{\varepsilon_0} = \sqrt{\frac{A}{C}}\left(-B + \frac{M_{11}}{M_{12}}\right) \\
\gamma_0 =& \frac{\Sigma_{22_0}}{\varepsilon_0} = \frac{1}{\sqrt{AC}}\left[(AB+C)^2 - 2AB\left(\frac{M_{11}}{M_{12}}\right) + A\left(\frac{M_{11}}{M_{12}}\right)^2\right]\,.
\end{aligned}$$

Simulation of this quadrupole scan was performed with the accelerator simulation code *elegant*, software for accelerator design and simulation code developed at Argonne National Laboratory (ANL) [11]. Since the synchrotron radiation interferometer location is downstream of the dipole MJA3C08, we can measure the Twiss parameters and emittance upstream quadrupole MQK3C04 using the harp IHA3C05. Harp, or wire scanners, are device used to measure transverse size of the electron beam. In harps at CEBAF, a thin wire is stepped through the particle beam. At each step, the wire intercepts a small part of beam, and the interaction rate is measured as a function of the wire's position. This is then plotted as intensity vs wire position. The signal can be fitted to a Gaussian to calculate the RMS beam size, and the center of this Gaussian provides the beam position.

We used IHA3C05 to measure the beam size in horizontal plane. The real time measurement is done by program *qsUtility* in the CEBAF control system which acquires and analyzes the quadrupole scan data. Initial simulations were performed with *elegant* and python script. Figure 20 shows the Gaussian fit plot of the signal intensity vs harp position. The x-axis represents the position of the wire scanner as it moves through the beam over a small range. The y-axis represents the measured intensity of the interaction between the beam and the harp wire at each position. The peak of the signal (beam center) is around 0.0335 m (33.5 mm), and the width of the Gaussian fit gives the RMS beam size.

Figure 21 is a result of the quadrupole scan to measure the emittance and Twiss parameters in the horizontal plane, plotting the measured values of the beam size squared at different quadrupole strengths K.

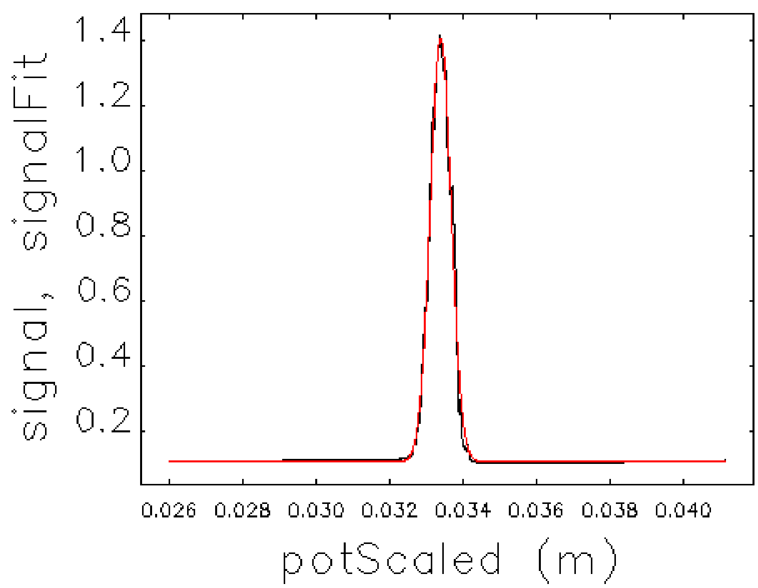

Figure 20. Typical signal fit at IHA3C05 in the horizontal plane, performed with the program *qsUtility* in the CEBAF control system.

Using the quadratic fit of the form

$$\sigma_{\mathrm{w}}^2(K) = A(K-B)^2 + C\,. \tag{56}$$

This represents the beam size squared vs quadrupole strength as parabola [12].

Table 2. Comparison of Design and Measured Twiss Parameters.

Parameter	**Emittance** [m − rad]	β **[m]**	α
Design	2.7261×10^{-10}	3.1897×10^{1}	-3.7897
Measured using python script	2.2164×10^{-10}	3.3475	-4.2036×10^{-1}

Table 3. Comparison of Design and Measured Twiss Parameters with *qsUtility*.

Parameter	**Emittance** [m − rad]	β **[m]**	α
Design	2.7261×10^{-10}	3.1897×10^{1}	-3.7897
Measured using *qsUtility*	1.4636×10^{-9}	3.8391×10^{1}	-4.7692

Table 2 shows the comparison between designed values for Twiss parameter and measured values using python script. Table 3 shows the comparison between Designed values for Twiss parameter and measured values using *qsUtility*. Figure 23 shows the transverse phase space plot. The measured ellipse is approximately similar to the design phase space. It also indicates that phase space ellipse is more focused since the emittance is low.

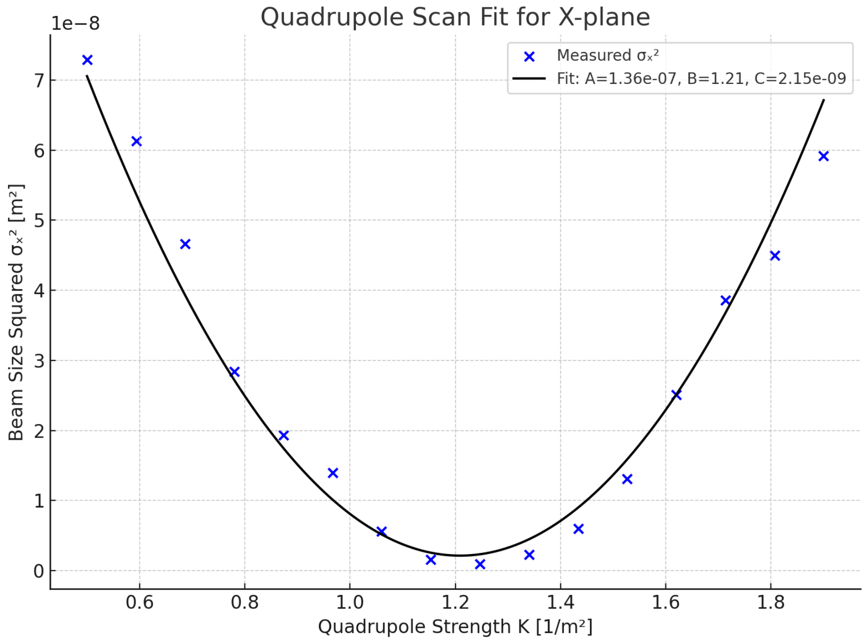

Figure 21. Beam size squared as a function of quadrupole field strength in the X-plane using Python script.

As we know, Synchrotron radiation is emitted when electrons follow a curved trajectory at relativistic speed. The transverse emittance is affected by synchrotron radiation at higher energies.

$$\Delta\varepsilon \approx 2 \times 10^{-27} \left(\frac{\gamma^5}{\rho \ [\mathrm{m}]^2} \right) \langle \mathscr{H} \rangle \,. \tag{57}$$

This equation tells us how there is increase in geometric emittance due to synchrotron radiation [8]. ρ is the radius of curvature of the bending magnet where larger the radius we see less effect of synchrotron radiation. γ is the Lorentz factor which is proportional to the electron beam energy. The emittance growth scales as γ^5. Like emittance we also see increase in the energy

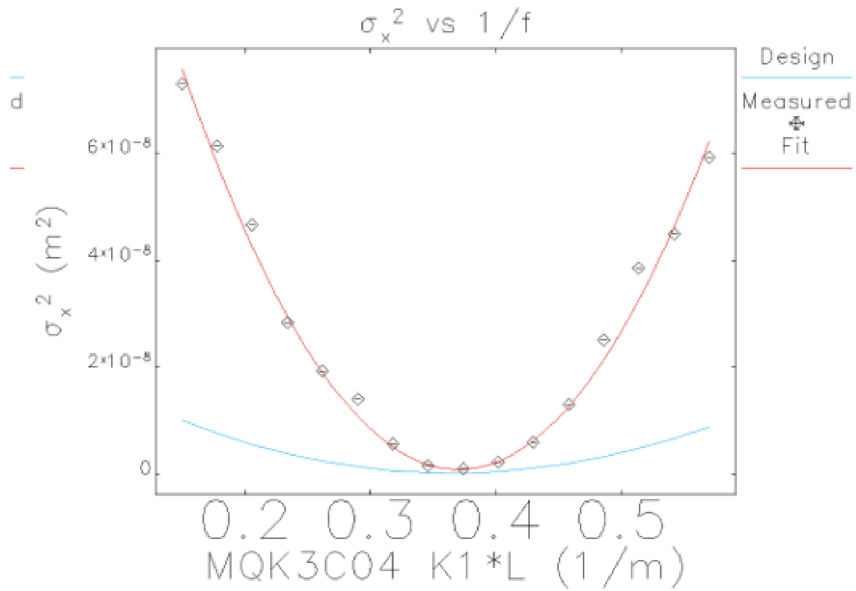

Figure 22. Beam size squared as a function of quadrupole field strength in the X-plane done by *qsUtility*.

spread of the electron beam:

$$\sigma_E^2 \approx 1.2 \times 10^{-33}\ \mathrm{GeV}^2 \left(\frac{\gamma^7}{\rho\ [\mathrm{m}]^2} \right) . \tag{58}$$

This equation tells us that energy spread scales γ^7 due to increase in beam's energy. Since the total beam size equals to the emittance contribution and dispersion contribution. The total beam size increases at higher energies [8].

The total beam size at any location can be expressed as:

$$\sigma_x^2 = \underbrace{\beta_x \varepsilon_x}_{\text{emittance contribution}} + \underbrace{\left(\eta_x \frac{\Delta p}{p} \right)^2}_{\text{dispersion contribution}} . \tag{59}$$

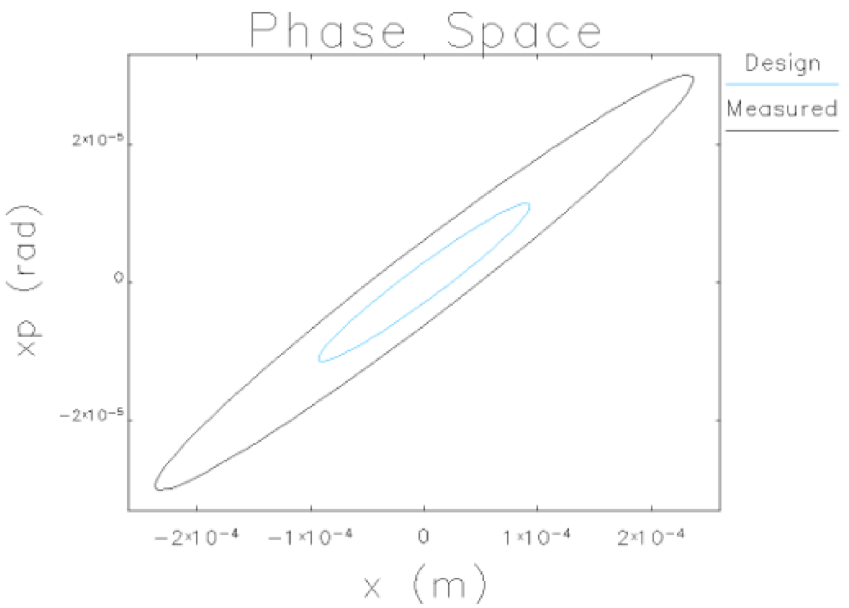

Figure 23. Transverse phase space plot: The area of ellipse is proportional to the geometric emittance of the beam.

Dispersion (η_x) tells us how much there is shift in beam position due to momentum deviations. Increase in energy spread with a large dispersion increases the beam size at high energy location. Relative momentum spread $\left(\frac{\Delta p}{p}\right)$ also represents energy spread with the beam. Therefore the beam size increases at higher energies due to larger dispersion contribution:

$$\sigma_x = \sqrt{\beta_x \varepsilon_x + \left(\eta_x \frac{\Delta p}{p}\right)^2}. \tag{60}$$

CHAPTER 5

FOURIER OPTICS AND SRW SIMULATIONS IN SIREPO

5.1 SIREPO AND SYNCHROTRON RADIATION WORKSHOP

To test SRI, a series of simulations have been performed with *SRW Sirepo* which is a web-based graphical user interface (GUI) for simulation of synchrotron radiation and X-ray optics [13]. Sirepo includes the software Synchrotron Radiation Workshop (SRW), a commonly used computer simulation code at the back-end of the software. This SRI system is designed has simple Young's double slit layout shown in Figure 24.

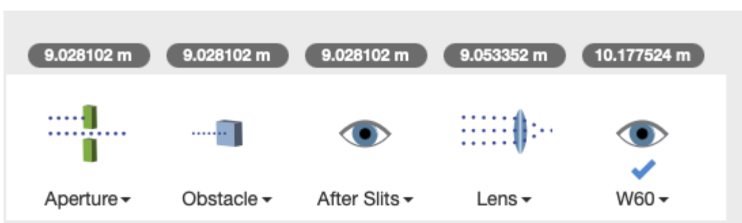

Figure 24. Young's double slit layout in SRW Sirepo. The layout consists of an aperture and obstacle that create a double slit, the drift after the slit, a lens, and watchpoint (W60).

The layout of Young's double slit consists of an aperture, obstacle, after-slit drift, lens, and watch point. The distance between aperture and obstacle is 9.028102 m. The distance between obstacle and after slits is 9.028102 m. The distance between the after slits and lens is 9.053352 m. The distance between lens and watch point is 10.177524 m. The beam properties of CEBAF accelerator is given in Table 4. The beam parameters based on which the simulations for taken are given in Tables 5 and 6.

Table 4. Design CEBAF Beam Properties in Hall C on First Pass

Energy [GeV]	2.303
Current [A]	2×10^{-5}
RMS Energy Spread	1.33×10^{-5}
Beam Definition by	Twiss parameters

Table 5. Design Horizontal Twiss Parameters for MJA3C08.

Emittance [ε_x] (nm)	0.17835
Beta [β_x] (m)	20.038
Alpha [α_x] (rad)	-2.54985
Dispersion [D_x] (m)	3.70165
Dispersion Derivative [D'_x] (rad)	-0.51426

Table 6. Design Vertical Twiss Parameters for MJA3C08.

Emittance [ε_y] (nm)	0.18511
Beta [β_y] (m)	21.0526
Alpha [α_y] (rad)	2.29209
Dispersion [D_y] (m)	0.0
Dispersion Derivative [D'_y] (rad)	0.0

In principle the synchrotron light passes through the double slits created by aperture and obstacle, passes through the lens and displays the interference pattern on the watchpoint or screen. By observing this interference pattern we can measure the visibility and we can calculate the beam size and energy spread. Using the SRW Sirepo simulations we can measure the visibility by identifying the maximum intensity ($I_{\max}$) and minimum intensity ($I_{\min}$) in the intensity plot. The intensity plots depends on the slit separation and slit width. By varying the slit separation and slit width we can influence the interference pattern. To get accurate measurement we want high intensity and more peaks in the intensity plot. The main goal of this simulations are to identify the ideal slit separation and slit width for getting maximum intensity and good amount of visibility to extract peaks from simulated intensity plots. Visibility changes depending upon slit separation and slit width. This SRW simulation in Sirepo is extracted in the form of an Excel file and in image formate. Many simulations were performed to get an ideal slit separation and slit width. Another important factor in this simulation is the sampling size. Sampling size refers to the spatial length and resolution of the simulation grid where the radiation field is calculated. sampling size also affects the accuracy of the simulations. The dimension of the simulation grid has horizontal and vertical range (size) with a discrete number of points across each axis which can be also refer as pixel counts. In this simulation, default sampling size was 10.5 mm with 500 sampling points. This ensure the finer details about interference pattern and the accuracy of the simulation. Simulations were divided into four sets: only changing slit separation, only changing slit width, only changing sampling size, and only changing energy spread.

Energy spread of the beam is determined by dispersion and dispersion size. The beam size is

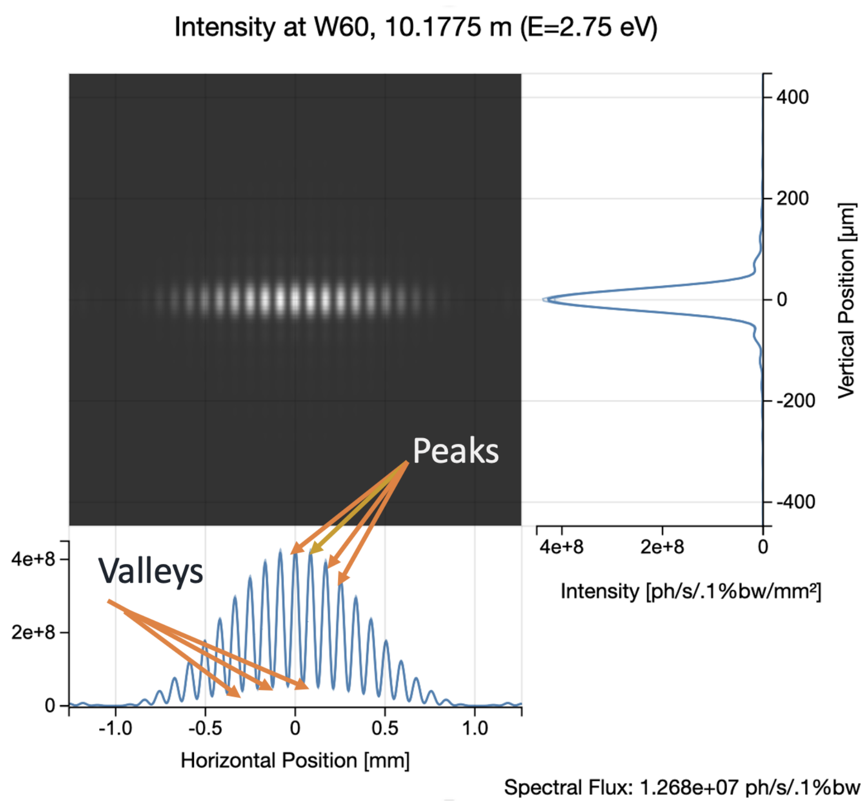

Figure 25. Visibility from peaks and valleys: Using these peaks and valleys we can calculate the visibility.

determine by using the given wavelength, slit geometry and visibility:

$$\sigma_y = \frac{\lambda SD}{\pi SG}\sqrt{0.5\ln\left(\frac{1}{V_y}\right)}, \tag{61}$$

where λ is the wavelength, SD is the slit distance, SG is the slit gap, and V_x is the visibility function.

Tables 7 and 8 show SRI simulation results for varying slit width and slit separation, respectively, with a sampling location at 10.5 m. When varying the slit width while keeping the slit separation fixed at 7 mm, the calculated energy spread for a 0.5 mm slit width is 9.42×10^{-6} with an error of 3.88×10^{-6}. For a slit width of 0.6 mm and the same separation, the energy spread is 9.14×10^{-6} with an error of 4.16×10^{-6}.

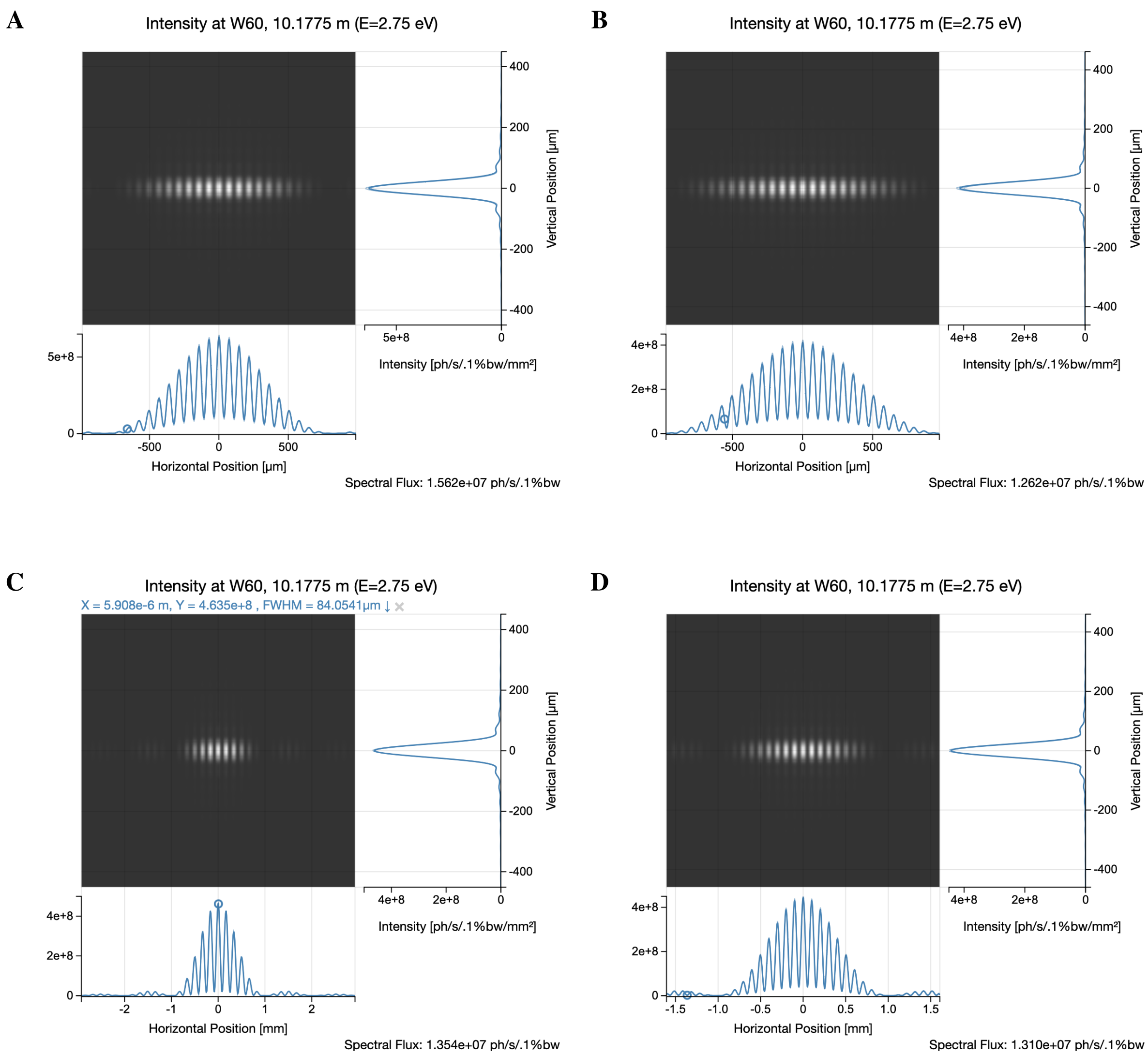

Figure 26. Slit separation and width scan. *(A)* 7 mm separation, 0.6 mm width, *(B)* 7 mm separation, 0.5 mm width, *(C)* 3 mm separation, 0.5 mm width, and *(D)* 5 mm separation, 0.5 mm width.

Table 8 also presents simulation results for varying slit separation during the first pass. With a fixed slit width of 0.5 mm, the calculated energy spread for a 7 mm slit separation is 1.36×10^{-5} with an error of 3.00×10^{-7}. By iterating over different combinations of slit width and separation, we identified an optimal configuration that provides higher intensity, good fringe visibility, and a low measured energy spread error.

Table 7. Only Changing Slit Width for First Pass.

Slit SP (mm)	**Width** (mm)	**Sample** size (m)	**Sim ES**	**CAL ES**	**Max** Pixel/s	**Error**
7	0.3	10.5	1.33×10^{-5}	9.38×10^{-6}	134	3.92×10^{-6}
7	0.4	10.5	1.33×10^{-5}	9.41×10^{-6}	200	3.89×10^{-6}
7	0.5	10.5	1.33×10^{-5}	9.42×10^{-6}	323	3.88×10^{-6}
7	0.6	10.5	1.33×10^{-5}	9.14×10^{-6}	475	4.16×10^{-6}
7	0.7	10.5	1.33×10^{-5}	9.25×10^{-6}	653	4.05×10^{-6}
7	0.8	10.5	1.33×10^{-5}	9.22×10^{-6}	858	4.08×10^{-6}

Table 8. Only Changing Slit Separation for First Pass.

Slit SP (mm)	**Width** (mm)	**Sample** size (m)	**Sim ES**	**CAL ES**	**Max** Pixel/s	**Error**
3	0.5	10.5	1.33×10^{-5}	1.72×10^{-5}	798	3.90×10^{-6}
4	0.5	10.5	1.33×10^{-5}	1.62×10^{-5}	779	2.90×10^{-6}
5	0.5	10.5	1.33×10^{-5}	1.38×10^{-5}	765	5.00×10^{-7}
6	0.5	10.5	1.33×10^{-5}	1.38×10^{-5}	737	5.00×10^{-7}
7	0.5	10.5	1.33×10^{-5}	1.36×10^{-5}	710	3.00×10^{-7}
8	0.5	10.5	1.33×10^{-5}	1.35×10^{-5}	680	2.00×10^{-7}

5.2 FOURIER OPTICS IN SIREPO

To understand how the SRI simulations have been done, we need to have some understanding of Fourier optics specifically used in Sirepo [14]. Fourier optics tells us how the light waves interact with the optical systems using Fourier transforms. In this the light is treated as a combination of spatial frequencies. The rate of variation of intensity in an wave as a function of spatial position is called spatial frequency. To understand how light waves interact with the optical systems we start by writing a wave equation for a monochromatic wave:

$$\nabla^2 U(x,y,z) + k^2 U(x,y,z) = 0\,, \tag{62}$$

where

- $U(x,y,z)$: Scalar field (e.g., electric or magnetic field component of the wave),
- $k = \frac{2\pi}{\lambda}$: Wavenumber, with λ as the wavelength, and
- ∇^2: Laplacian operator.

For a wave propagating along the z-axis, $U(x,y,z)$ is a function of z which is in longitudinal coordinate and x,y in transverse coordinates. The wave propagates in the z-direction with small angular deviations from the axis. This is called the paraxial approximation. The field $U(x,y,z)$ is expressed as:

$$U(x,y,z) = \Psi(x,y,z)\exp(-ikz)\,, \tag{63}$$

where

- $\exp(-ikz)$: Represents the oscillating plane wave along z, and

- $\Psi(x,y,z)$: field variation in the transverse plane.

Substituting $U(x,y,z) = \Psi(x,y,z)\exp(-ikz)$ into the wave equation,

$$\left[\nabla^2\Psi - 2ik\frac{\partial\Psi}{\partial z}\right] + \frac{\partial^2\Psi}{\partial z^2}\exp(-ikz) = 0\,. \tag{64}$$

Since $\Psi(x,y,z)$ gradually varies, $\frac{\partial^2\Psi}{\partial z^2}$ is negligible compared to $2ik\frac{\partial\Psi}{\partial z}$. This gives:

$$\nabla_\perp^2\Psi - 2ik\frac{\partial\Psi}{\partial z} = 0\,, \tag{65}$$

where $\nabla_\perp^2 = \frac{\partial^2}{\partial x^2} + \frac{\partial^2}{\partial y^2}$ is the transverse Laplacian.

This is the paraxial wave equation. To compute the field at a distance $z = L$, we can use Fresnel diffraction integral. Let $U(x',y',0)$ represent the field in the source plane ($z = 0$), and we wish to compute $U(x,y,z = L)$ in the observation plane at $z = L$. The Fresnel diffraction formula relates the two fields:

$$U(x,y,L) = \frac{\exp(ikL)}{i\lambda L}\int_{-\infty}^{\infty}\int_{-\infty}^{\infty} U(x',y',0)\exp\left(\frac{ik}{2L}\left[(x-x')^2 + (y-y')^2\right]\right)dx'dy'\,, \tag{66}$$

where

- $U(x',y',0)$: Field in the source plane,
- $U(x,y,L)$: Field in the observation plane, and
- $\frac{\exp(ikL)}{i\lambda L}$: Pre-factor from free-space propagation.

This equation shows that the field at $z = L$ is a convolution of the initial field with a quadratic phase kernel:

$$K(x,y) = \exp\left(\frac{ik}{2L}\left(x^2+y^2\right)\right) \tag{67}$$

This quadratic phase kernel tells us about the phase curvature of wavefront as it propagates in free space through any optical systems [14].

- $k = \frac{2\pi}{\lambda}$: Wavenumber,
- L: Propagation distance,
- $\frac{k}{2L}$: Controls the curvature induced by free-space propagation.

This kernel represents how the phase of the wavefront evolves due to spherical curvature during propagation.

The Fresnel free-space propagator is a mathematical operator that transforms the field from one plane to another. It is based on the *Fresnel diffraction integral*:

$$U(x,y,L) = \mathscr{P}_{\text{Fresnel}}[U(x',y',0)]\,, \tag{68}$$

where

$$\mathscr{P}_{\text{Fresnel}}[U(x',y',0)] = \frac{\exp(ikL)}{i\lambda L}\int_{-\infty}^{\infty}\int_{-\infty}^{\infty} U(x',y',0)\exp\left(\frac{ik}{2L}\left[(x-x')^2+(y-y')^2\right]\right)dx'dy' \tag{69}$$

This can be written in the *Fourier domain* as:

$$\tilde{U}(f_x,f_y,L) = \tilde{U}(f_x,f_y,0)\exp\left(-i\frac{\pi\lambda L}{2}\left[f_x^2+f_y^2\right]\right)\,, \tag{70}$$

where

- $\tilde{U}(f_x, f_y, L)$: Fourier transform of the field at $z = L$, and
- $\exp\left(-i\frac{\pi\lambda L}{2}\left[f_x^2 + f_y^2\right]\right)$: Fourier domain propagation kernel.

This Fresnel propagator includes a quadratic phase term which describes the curvature of the wavefront as it propagates [14]:

$$\exp\left(\frac{ik}{2L}\left[(x-x')^2 + (y-y')^2\right]\right) . \tag{71}$$

This accounts for spherical wavefront curvature due to propagation in free space and the diffraction effects resulting from the aperture or obstacle. This quadratic phase kernel transforms a wavefront by introducing curvature in either the spatial or Fourier domain:

- In the spatial domain, it modifies the phase profile of the wave.
- In the Fourier domain, it applies a frequency-dependent phase shift:

$$H(f_x, f_y) = \exp\left(-i\frac{\pi\lambda L}{2}\left(f_x^2 + f_y^2\right)\right) , \tag{72}$$

where $H(f_x, f_y)$ is the Fourier domain representation of the free-space propagator. This quadratic phase kernel governs the propagation, diffraction, and focusing behavior of optical wavefronts. The Fresnel integral needs convolution in the spatial domain between the input field and a quadratic phase kernel. Using the convolution theorem, the Fresnel propagation is computed efficiently in the Fourier domain:

$$\tilde{U}(f_x, f_y, L) = \tilde{U}(f_x, f_y, 0)H(f_x, f_y) , \tag{73}$$

where $H(f_x, f_y)$ is the *Fresnel kernel*:

$$H(f_x, f_y) = \exp\left(-i\frac{\pi\lambda L}{2}\left[f_x^2 + f_y^2\right]\right) . \tag{74}$$

Conversion to the spatial domain is done via the inverse Fourier transform:

$$U(x, y, L) = \mathscr{F}^{-1}\left[\tilde{U}(f_x, f_y, L)\right] . \tag{75}$$

5.2.1 Nyquist-Shannon Theorem: Sampling

To ensure proper sampling, use the sampling criterion:

$$N = \left\lceil \frac{p\Delta\theta^2 R}{\lambda} \right\rceil , \tag{76}$$

where

- $\Delta\theta$: Angular resolution,
- R: Radius of curvature,
- λ: Wavelength,
- p: Sampling parameter ($p \geq 1$).

This ensures the field is sampled finely enough to capture all oscillations and avoid aliasing.

The Nyquist-Shannon sampling theorem states that a continuous signal can be completely represented by its samples if the sampling frequency is at least twice the highest frequency present in the signal. This critical sampling frequency is known as the Nyquist frequency. Undersampling can cause to aliasing, where high frequencies can get mixed up into lower frequencies and can effect the propagated field [14].

The Fourier optics behind SRI simulations revolves around this free-space propagator and quadratic phase kernel to describes in behavior of the propagating wave through each optical systems. This is done by the following three steps. Using the free-space propagator, 1) Take the Fourier transform of the initial field. 2) Multiplying it by the Fresnel propagation kernel in the Fourier domain. 3) Performing the inverse Fourier transform to return to the spatial domain. Mostly this steps are easily done by using powerful numerical methods which is done by Sirepo very efficiently [13].

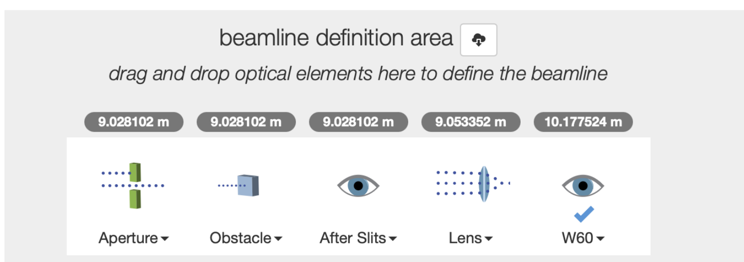

Figure 27. Optical Beamline setup for SRI: aperture, obstacle, after slit, lens and watchpoint (W60).

Figure 27 includes the setup for these simulations, including an aperture and obstacle that combine to create interference slits, the after slit drift, lens, and the observation plane (W60).

5.2.2 Electric Field At the Aperture

The aperture modifies the initial electric field $U_{\text{initial}}(x,y)$ by multiplying it with the aperture function $A(x,y)$:

$$U_1(x,y) = A(x,y)U_{\text{initial}}(x,y)\,, \tag{77}$$

where

- $A(x,y) = \text{rect}\left(\frac{x}{w_x}\right)\text{rect}\left(\frac{y}{w_y}\right)$,
- w_x, w_y: Aperture dimensions,
- $U_{\text{initial}}(x,y) = \exp(-ikz)$: Plane wave incident on the aperture.

The Fourier transform of $U_1(x,y)$ becomes:

$$\tilde{U}_1(f_x,f_y) = \tilde{A}(f_x,f_y)\tilde{U}_{\text{initial}}(f_x,f_y)\,. \tag{78}$$

For the aperture:

$$\tilde{A}(f_x,f_y) = w_x w_y \text{sinc}(w_x f_x)\text{sinc}(w_y f_y)\,. \tag{79}$$

5.2.3 Propagation to the Obstacle

The Fresnel free-space propagation is described by:

$$U_2(x,y) = \frac{k}{2\pi i L_1}\exp(ikL_1)\int_{-\infty}^{\infty}\int_{-\infty}^{\infty} U_1(x',y')\exp\left(i\frac{k}{2L_1}\left[(x-x')^2+(y-y')^2\right]\right)dx'dy'\,. \tag{80}$$

Using the convolution theorem, this becomes

$$\tilde{U}_2(f_x,f_y) = \tilde{U}_1(f_x,f_y)H(f_x,f_y)\,, \tag{81}$$

where the Fresnel kernel $H(f_x, f_y)$ in the Fourier domain is

$$H(f_x, f_y) = \exp\left(-i\frac{\pi\lambda L_1}{2}\left[f_x^2 + f_y^2\right]\right). \tag{82}$$

5.2.4 Field At the Obstacle

The obstacle introduces an amplitude modulation is

$$U_{\text{obstacle}}(x,y) = O(x,y)U_2(x,y), \tag{83}$$

where $O(x,y)$ is the transmission function of the obstacle:

$$O(x,y) = 1 - \text{rect}\left(\frac{x}{w_0}\right)\text{rect}\left(\frac{y}{w_0}\right). \tag{84}$$

The Fourier transform of the field after the obstacle is:

$$\tilde{U}_{\text{obstacle}}(f_x, f_y) = \tilde{O}(f_x, f_y) * \tilde{U}_2(f_x, f_y), \tag{85}$$

where $\tilde{O}(f_x, f_y)$ is the Fourier transform of the obstacle function.

5.2.5 Field After the Double Slit

The double slit creates interference. Its transmission function is

$$T_{\text{slits}}(x,y) = \text{rect}\left(\frac{x - d/2}{w_s}\right) + \text{rect}\left(\frac{x + d/2}{w_s}\right). \tag{86}$$

The field after the double slit is

$$U_{\text{slits}}(x,y) = T_{\text{slits}}(x,y)U_{\text{obstacle}}(x,y)\,. \tag{87}$$

In the Fourier domain:

$$\tilde{U}_{\text{slits}}(f_x,f_y) = \tilde{T}_{\text{slits}}(f_x)\tilde{U}_{\text{obstacle}}(f_x,f_y)\,. \tag{88}$$

The Fourier transform of the double slit is:

$$\tilde{T}_{\text{slits}}(f_x) = 2w_s \text{sinc}(w_s f_x)\cos(\pi f_x d)\,. \tag{89}$$

5.2.6 Propagation to the Lens

The field propagates to the lens plane using the Fresnel free-space propagator:

$$\tilde{U}_{\text{lens}}(f_x,f_y) = \tilde{U}_{\text{slits}}(f_x,f_y)H(f_x,f_y)\,, \tag{90}$$

where:

$$H(f_x,f_y) = \exp\left(-i\frac{\pi\lambda L_2}{2}\left[f_x^2+f_y^2\right]\right)\,. \tag{91}$$

5.2.7 Lens Transformation

The lens introduces a quadratic phase term

$$U_{\text{lens}}(x,y) = U_{\text{slits}}(x,y)\exp\left(-i\frac{k}{2f}\left(x^2+y^2\right)\right). \tag{92}$$

In the Fourier domain:

$$\tilde{U}_{\text{lens}}(f_x,f_y) = \tilde{U}_{\text{slits}}(f_x,f_y)\exp\left(-i\frac{\pi\lambda f}{2}\left[f_x^2+f_y^2\right]\right). \tag{93}$$

5.2.8 Propagation to the Observation Plane

The field propagates to the observation plane (W60) using the Fresnel propagator:

$$\tilde{U}_{\text{W60}}(f_x,f_y) = \tilde{U}_{\text{lens}}(f_x,f_y)H(f_x,f_y), \tag{94}$$

where:

$$H(f_x,f_y) = \exp\left(-i\frac{\pi\lambda L_3}{2}\left[f_x^2+f_y^2\right]\right). \tag{95}$$

Finally, we perform the *inverse Fourier transform*:

$$U_{\text{W60}}(x,y) = \mathscr{F}^{-1}\left[\tilde{U}_{\text{W60}}(f_x,f_y)\right]. \tag{96}$$

5.2.9 Intensity At W60

The observed intensity at the W60 plane is:

$$I(x,y) = |U_{\mathrm{W60}}(x,y)|^2 . \tag{97}$$

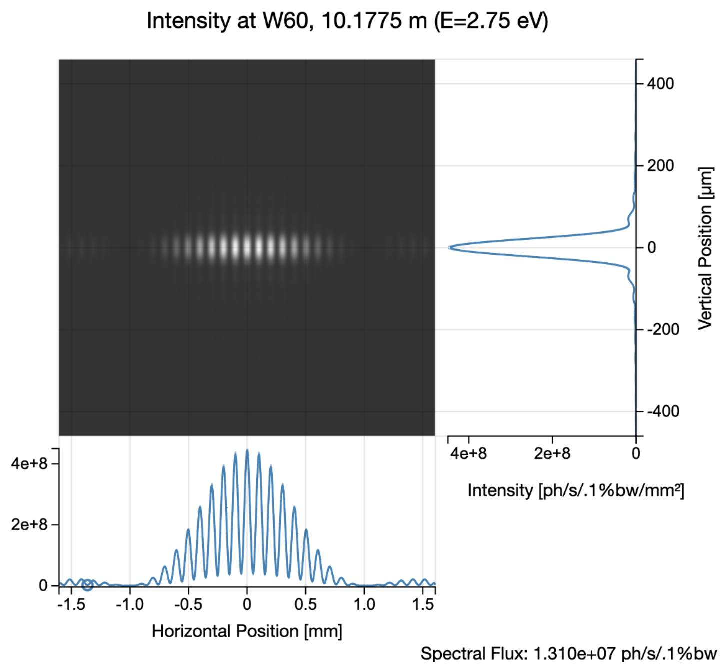

Figure 28. Final intensity at W60: Corresponding field propagated to the observation plane (W60) using the Fresnel propagator.

Figure 28 shows the final observed intensity at watchpoint (W60). If a signal $x(t)$ contains no frequencies higher than $f_{\max}$, it can be reconstructed exactly from its samples $x[n] = x(nT_s)$, where

T_s is the sampling interval and $f_s = \frac{1}{T_s}$ is the sampling frequency, provided:

$$f_s \geq 2 f_{\max} \,. \tag{98}$$

CHAPTER 6

SRI IMPLEMENTATION AND OPERATIONS

The Synchrotron Radiation Interferometer (SRI) is installed near dipole MJA3C08 in the Hall C transport line. The SRI device, ISR3C12, will be a new diagnostic device which will provide non-invasive continuous measurement of the electron beam energy spread. To implement the SRI, we must verify the values of Hall C correctors magnets and quadrupoles are set properly. Once we verified this values, we can perform a ZeroPos for the orbit lock at Hall C to establish an orbit reference. The orbit lock or closed-orbit lock is a feedback-based control for maintaining the electron beam at a specified ideal orbit. Since particles moving in an accelerator travel along the predefined closed orbit, or the reference orbit. Even small deviation from this orbit can cause problems for beam transport. The orbit lock system measures the beam position at different points in accelerator using Beam Position Monitors (BPMs). Any detected deviations are corrected through adjustments of correctors (steering magnets). After setting the ZeroPos orbit, we perform a quadrupole scan experimentally using *qsUtility* to measure Twiss parameters at 3C12.

In Section 4.3 we discussed how Twiss parameters are calculated using *elegant* simulations. Now using *qsUtility* we measure Twiss parameters experimentally. After measurement of Twiss parameters, we perform Hall C energy measurement to measure the absolute beam energy at 3C12. This beam is measured or monitored by the BPMs and dipoles by using Beam Energy Monitor software (*BEM*). Once all this initial measurements are taken we want to make sure that once synchrotron light is emitted from the electron beam, we get enough light on the camera. This is the most important task to perform. To ensure enough light on the camera first we need to steer beam through the orbit from 3C11 and 3C14. This will ensure that beam's orbit is close to zero. After this we have DC Servo motors to control the turning mirrors. Control on this turning mirrors are in the x, y and z direction. The values for x and y are estimated about 8.5mm. By adjusting the turning mirrors we make sure that synchrotron light appears on camera. If light does not appear on the camera by using turning mirrors we can steer the electron beam using correctors (steering magnets) and BPMs. Beam steering might perform by using upstream corrector: 3C07H for horizontal or 3C11V, 3C09V, and 3C07V for vertical. It it important to measure how much movement it takes to steer light off camera using turning mirror and how much movement it takes to steer light off camera using beam.

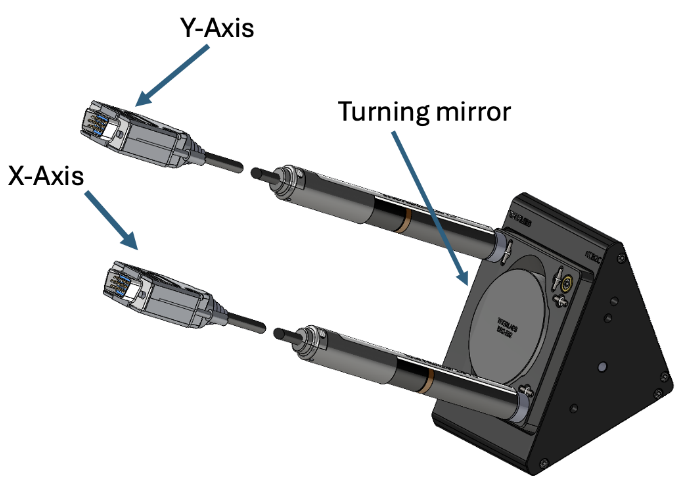

Figure 29. Turning mirror with DC servo motor actuators, used to control turning mirrors in three dimensions.

Once the light shows on the camera, we need to adjust the camera setting to optimize the image. The camera setting will make sure that image on the camera is more clear and well define interference fringes.

The main camera settings are the black level, gamma correction, exposure time (shutter speed), gain, and integration time.

Black Level: The black level is a baseline intensity which corresponds to black pixels in a particular region. This is the illumination level where pixels register no incoming light. By adjusting black level we can optimize the intensity of the image.

Gamma correction: Gamma correction is applied to an image when details are not clear in shadow region. It increases the brightness levels and improves the visibility in shadow region. It it very important that we see clear interference patterns on the screen. By adjusting gamma correction we can optimize the visibility in shadow region where some fringes are dark.

Exposure time: Exposure time is the duration the camera sensor is exposed to incoming light for capturing an image. A longer exposure time allows more light to hit the sensor, increasing image brightness.

Gain: Gain is the amplification of the sensor signal; it can be used to increase the brightness of the images increases without increasing exposure time, but it also introduces noise in the image. Optimizing the gain for the proper dynamic range to avoid saturation is important to optimize the overall system sensitivity. Gain can also affect the exposure time.

Integration time: Integration time specifies how long the sensor collects photons for a single image capture. Longer integration times increase sensitivity and brightness but can blur the image or can introduce saturation. It is very important to set proper integration time since it defines how much amount of light and how long the light should expose to the camera sensor.

After these camera settings, we also must set the Region of Interest (ROI). ROI refers the area where the interference pattern will form at the camera screen. Setting approximate ROI is very important since we need the interference pattern to be symmetric in X and Y direction. Setting wrong ROI adds noise in the interference pattern, and makes it difficult to analyze the interference fringe pattern. Beam current will be set to 5 μA initially and will increase to 10 μA when all measurements are done accurately for 5 μA. Data acquisition and analysis are performed by LabView and Python code.

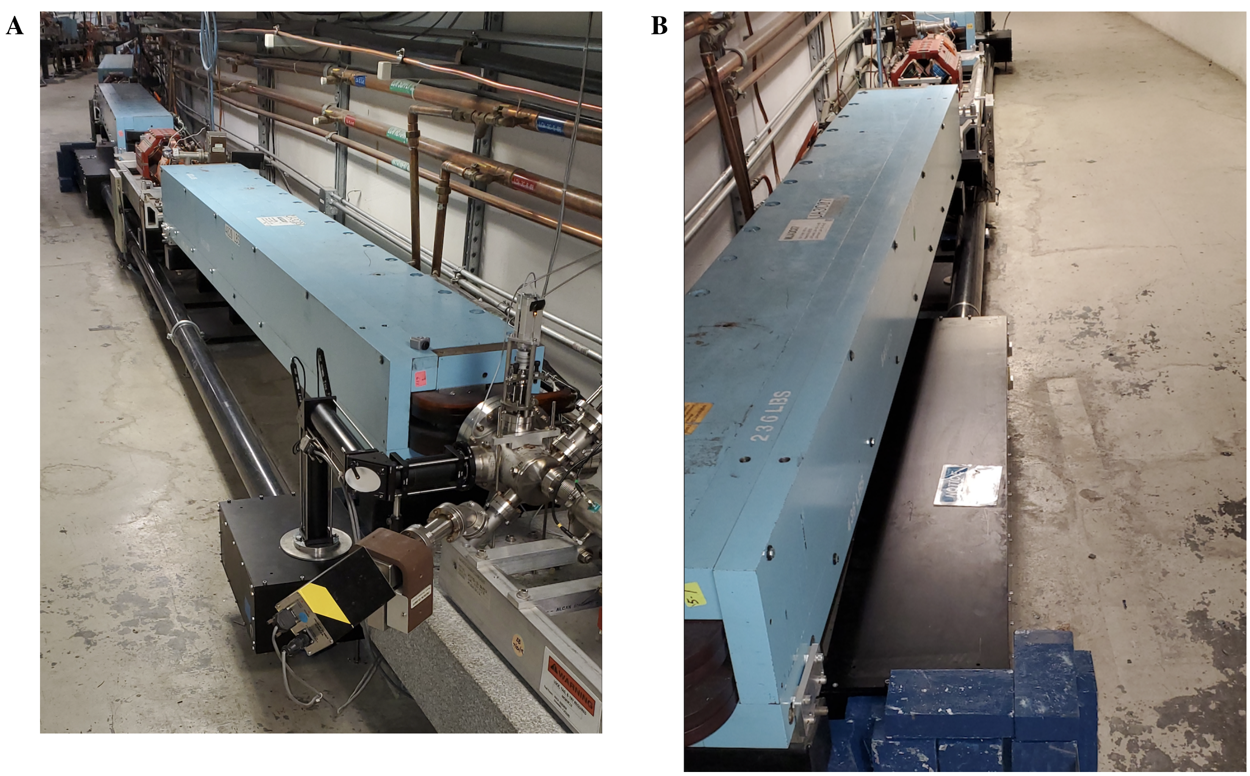

Figure 30. The synchrotron radiation interferometer (SRI) installed at dipole MJA3C08. *(A)* includes box 1 with the viewport and 3 turning mirrors. *(B)* includes box 2 with the polarizer, bandpass filter, lens, slit stage and camera.

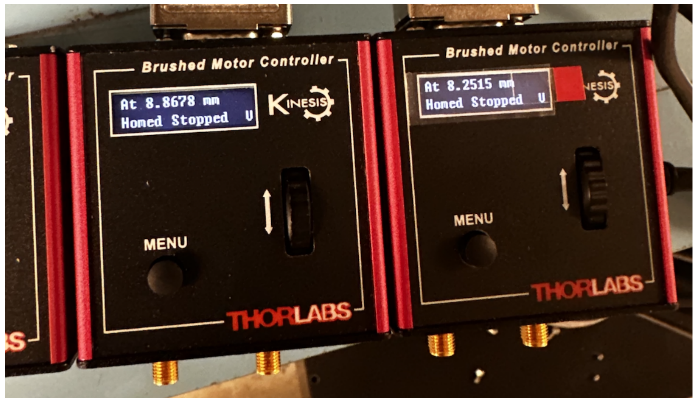

Figure 31. DC servo motor for controlling the turning mirror in three dimensions. Image shows initial calibration values during laser alignment. The x direction was set to 8.8678 mm and the y direction was set to 8.2515 mm.

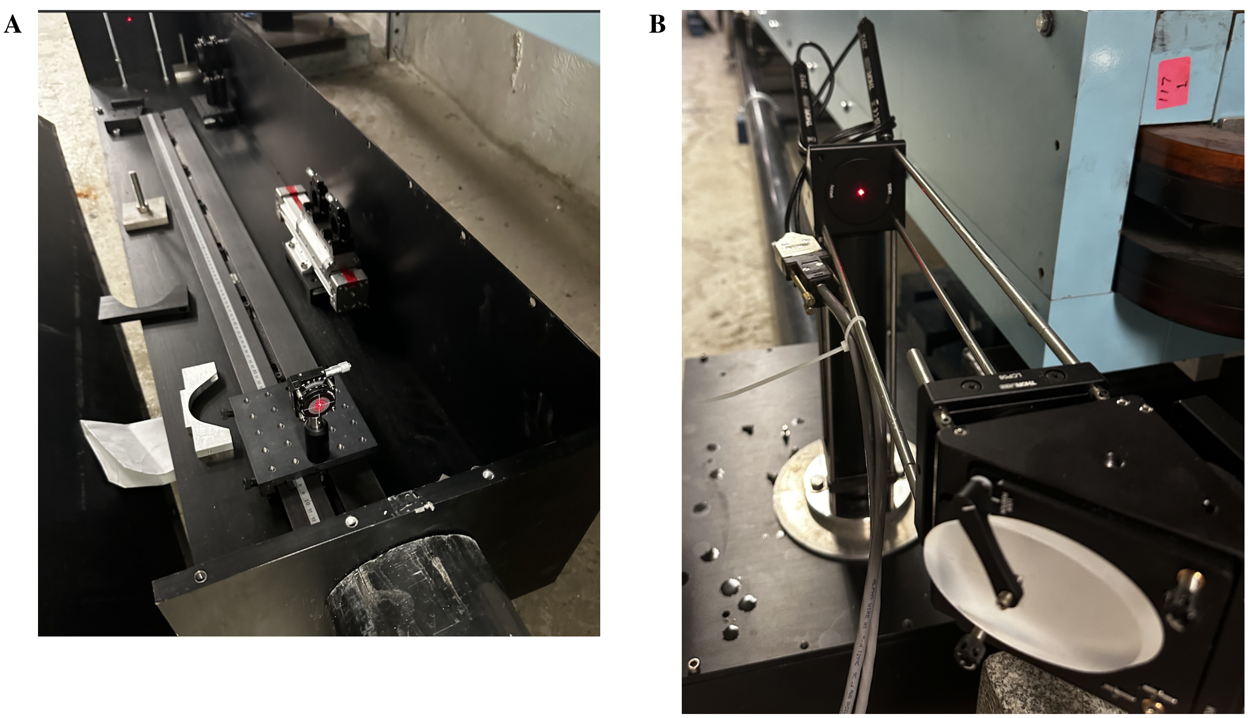

Figure 32. Laser alignment during installation of SRI. *(A)*: Lens on optical track and camera in box 2. *(B)*: Laser alignment through turning mirrors in box 1.

CHAPTER 7

DATA ACQUISITION AND DATA ANALYSIS

7.1 DATA ANALYSIS FOR SRI SIMULATIONS

In Chapter 5 we discussed about how SRI simulations were performed using Sirepo software for different slit separation and slit width. In this chapter we discuss the data analysis technique and data acquisition for simulated data from Sirepo. Two different ways are used in data analysis for the SRI simulated data. First is using LabVIEW software and second is a Python code. By comparing this both ways we can check the accuracy and consistency in the simulated results. Our main goal is to extract the value for visibility which allows us to calculate beam size and energy spread of the beam. The data in SRW Sirepo is extracted in the form of an Excel file and in the raw image format.

LabView (Laboratory Virtual Instrument Engineering Workbench) is a software platform for design system and development environment created by National Instruments (NI) [15]. This software is generally used for data acquisition or for instrument control system. The main advantage of this software is that it works very well with data acquisition devices (DAQs) and instruments and we can analyze data in real time. In SRI simulation, the intensity plot that we get is plotted against horizontal position (mm) vs intensity. This plot is extracted in array format via a CSV file. This array shows intensity points along each horizontal position. Now the main goal is to extract the $I_{\max}$ and $I_{\min}$ values from this array file to get visibility. To find this $I_{\max}$ and $I_{\min}$ values we need to detect the peaks and valleys in the intensity distribution. For this we use the wavelet method [16] available in LabView. The wavelet method is a signal processing technique used analyze and extract important features from data. In our case we will use this wavelet method for peak and valley detection in the intensity distribution. This wavelet method uses the Continuous Wavelet Transform (CWT) method which is also called wavelet transform [16]. This wavelet transform works on following equation:

$$W(a,b) = \frac{1}{\sqrt{a}} \int_{-\infty}^{\infty} f(t)\, \psi^*\Big(\frac{t-b}{a}\Big)\, dt\,, \tag{99}$$

where $\psi^*(t)$ is the complex conjugate of the wavelet function $\psi(t)$. a is the scaling factor and b is the *translation* factor which determines and controls the position of the wavelet. Once we find the peaks and valleys using continuous wavelet transform method we can identify the $I_{\max}$ and $I_{\min}$ to find the visibility. Now we compare wavelet method to conventional Gaussian method. For the Gaussian fitting we are using least-square method. By using this method it is easy to analyze the intensity distribution as well as finding beam width. We have a Gaussian function as

$$I(x) = Ae^{-\frac{(x-\mu)^2}{2\sigma^2}}\,, \tag{100}$$

where $I(x)$ is the intensity at position x, A is the peak intensity, μ is the center position and σ is the standard deviation The least-squares fitting method minimizes the difference between the measured data points I_i and the Gaussian model $I(x_i)$, which is typically given by:

$$S = \sum_i \left(I_i - Ae^{-\frac{(x_i-\mu)^2}{2\sigma^2}} \right)^2\,, \tag{101}$$

where S is the sum of squared residuals. In Fig. 21, we can see the LabView interface with an Gaussian fit. This simulated data is for a slit separation of 7 mm and slit width 0.6 mm, with an energy spread of 1.33×10^{-5}. By using the wavelet transform method we can see peaks and valleys are been extracted. Blue dotes represents peaks and blue squares represent valleys. On the right side we have all the beam parameters like beam size, dispersion and energy spread along with the beam's Twiss parameters. On the left side, we have extracted $I_{\max}$ and $I_{\min}$ along with $I_{\max}$ and $I_{\min}$ residues.

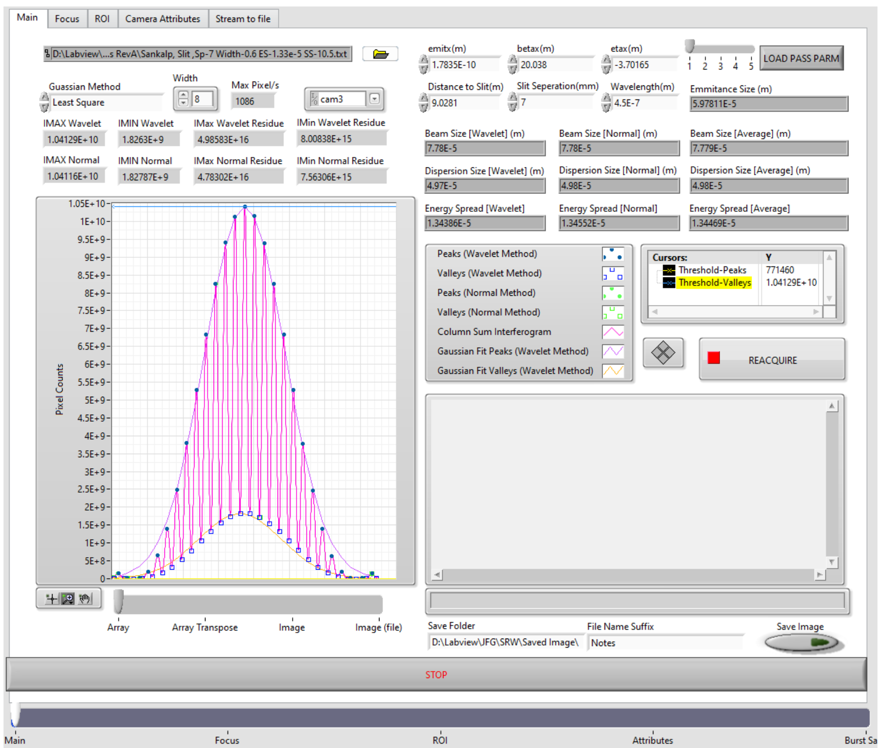

Figure 33. LabView interface with Gaussian fit: Simulated for slit separation of 7 mm and slit width 0.6 mm with an energy spread of 1.33×10^{-5}.

Once the $I_{\max}$ and $I_{\min}$ is found we measure visibility. Using visibility now we find beam size and energy spread. As we can see in Fig. 33, measured energy spread is $1.343\,86 \times 10^{-5}$ which is very close to input energy spread of 1.3×10^{-5} from Sirepo simulations. This energy spread and beam parameters are calculated using the formulas mentioned in Chapter 2. This confirms that the wavelet method and Gaussian Least-Fit method works pretty accurately. Another way to analyze data from Sirepo is using Python code. We can use Python to analyze same data from Sirepo and see the results. We also compare both two method to show the accuracy of simulated data and which will also help in DAQ for real time measurements.

The raw data file which is in CSV format is converted to array file. Same conversion is was done for LabView. This array file is then uploaded to python script to extract the peaks and valleys to get $I_{\max}$ and $I_{\min}$. Detection of peaks and valleys is done with the wavelet transform method, which is same as used in LabView. Once this peaks and valleys are determine, mean and standard deviation of an array is determine using `calc_noise(arr)` in the code. Again we use conventional Gaussian fit function to fit the data from Sirepo simulation.

$$\text{Gaussian}(x, \text{amp}, \mu, \sigma) = Ae^{-\frac{(x-\mu)^2}{2\sigma^2}}, \tag{102}$$

where A = amplitude, μ = mean, σ = standard deviation. This Gaussian fit helps to distinguish individual peak. Also it gives a good estimation of the peak intensity, position and width of the beam profile. But this Gaussian fit does not give estimation of other beam parameters like visibility, energy spread and effects of the slit separation on the interference pattern. Since in LabView we used the formulas from Chapter 2, we can use another method to determine beam parameters. We can use an generalized diffraction fitting model to incorporate physical beam parameter [3]. The diffraction fitting model is described as

$$y(x) = A(x, x_0, I_b, I_0, a, b, V, \varphi) = I_b + I_0 \left(\frac{\sin a(x - x_0)}{a(x - x_0)} \right)^2 (1 + V \cos(b(x - x_0) + \varphi)), \tag{103}$$

where a, b, and φ depend on the size of the slits, the slit separation D, and the phase difference of the light. I_b is a background noise. I_0 is determined by the intensity of the synchrotron light source. x_0 is the shift of the interferogram with respect to the origin of the image axis x. V is the visibility of the interference pattern. we can use a simplified version of this formula for our diffraction fit model. The generalized model function used is

$$\text{diff\_model}(x, IN, I0, A, B, D, V, F) = IN + \left(I0\,\text{sinc}^2\left(\frac{A(x-B)}{\pi}\right)\right) \times \left[1 + V\cos\left(D(x-B) - F\right)\right], \tag{104}$$

where IN = Background intensity, $I0$ = intensity, A, B, D, V, F is fitting parameters. As we can see in Figs. 34A and 34B, by using the fitting model we have a good fit 7 mm slit separation and 0.6 mm and 0.5 mm slit width. This tells us that the fitting model accurately distinguishes the peaks and valleys of the interference pattern and calculated the visibility. The visibility for 7 mm slit separation and 0.6 mm is $V = 0.75$ and visibility for 7 mm slit separation and 0.5 mm slit width is $V = 0.72$.

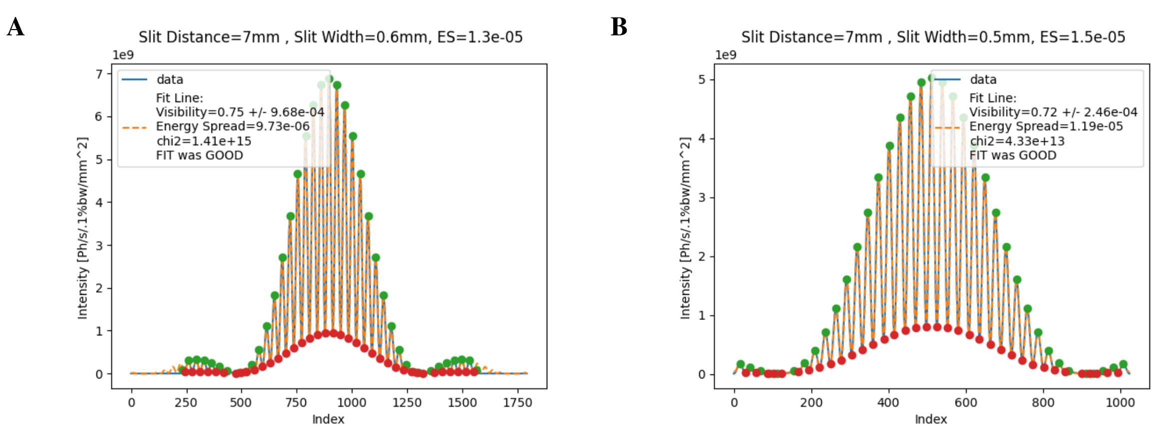

Figure 34. Gaussian Fit using model function and Python script: Simulated for a slit separation of 7 mm and a slit width 0.6 mm *(A)* or slit width 0.5 mm *(B)* with an energy spread of 1.33×10^{-5}.

CHAPTER 8

DISCUSSION AND FUTURE WORK

The Synchrotron Radiation Interferometer (SRI) is currently installed near dipole MJA3C08 in the Hall C transport line. This newly developed diagnostic device, designated ISR3C12, enables non-invasive, continuous measurement of the electron beam energy spread for upcoming hypernuclear physics experiments at CEBAF.

During the development of the SRI, two major challenges were encountered. The first was the selection of suitable optical elements optimized for 450 nm, as the camera used in the system has its highest quantum efficiency (75%) at this wavelength. Therefore, it was essential to choose optical components with maximum transmission at 450 nm to ensure optimal system performance.

The second challenge involved optimizing the optical transport simulation using *Sirepo*. Simulations were conducted with a sampling size of 10.5 mm. Determining the appropriate sampling size was non-trivial, as it significantly affected the visibility and number of interference fringes. A key goal of the simulation was to obtain a high-intensity interference pattern with multiple peaks. This optimization required a solid understanding of the Fourier optics principles that underpins the simulation.

Future implementation of the SRI involves routine quadrupole scan using the *qsUtility* tool to experimentally determine the Twiss parameters at 3C12 as input to energy spread calculations. Once the Twiss parameters are measured, energy measurements will be carried out in Hall C to determine the absolute beam energy at this location. These measurements will be supported by Beam Position Monitors (BPMs) and dipole magnets, using the Beam Energy Monitor (BEM) software. Ensuring that sufficient synchrotron light reaches the camera is another critical aspect. This will be achieved by adjusting a turning mirror via DC servo motors.

Once the synchrotron light appears on the camera, its settings will be tuned to optimize image quality. Initially, the beam current will be set to 5 μA, and increased to 10 μA once all measurements at 5 μA are completed and verified for accuracy. Data acquisition and preliminary analysis will be conducted using *LabVIEW*, with further data analysis performed using *Python*. The results will be compared against SRW *Sirepo* simulations conducted for various slit sizes.

Energy spread measurements will first be carried out for the first beam pass, at an electron beam energy near 2 GeV. If successful, the system will be extended to higher beam passes and electron beam energies. The SRI also holds potential for future beam studies. These may include investigating changes in beam size using slits with fixed separation but varying slit openings, and analyzing fringe visibility by altering slit separation at different beam energies. This work has focused on the initial development of the SRI system, including its installation, design, simulation, construction, and commissioning.

CHAPTER 9

CONCLUSIONS

In this work, a Synchrotron Radiation Interferometer (SRI) was simulated and implemented along the Hall C transport line near the dipole magnet MJA3C08. The system takes advantage of synchrotron light emitted by the electron beam as it undergoes bending in the dipole magnetic field, and employs a Young's double-slit interferometer to analyze the spatial coherence of this radiation. The primary objective of this study was to measure the transverse beam size and infer the energy spread of the electron beam using interference fringe visibility.

The beam's transverse size σ_{beam}, emittance ε_x, Twiss parameters, and dispersion η_x were obtained by applying the Van Cittert–Zernike theorem and conducting Twiss parameter and emittance measurements with a quadrupole scan method in the Hall C line. These parameters enabled the calculation of energy spread σ_δ, with optimal sensitivity achieved due to overall optics design and interferometer placement at a dipole with high dispersion. The optical transport system was carefully designed to maximize throughput and ensure high-quality imaging at an operating wavelength of 450 nm. Key optical components included insertable and turning mirrors, a polarizer, a bandpass filter, a focusing lens, and a camera. Each optical element was selected based on its transmission and reflectivity to preserve the coherence and intensity of the synchrotron light.

To optimize the interferometer design, simulations were performed using a software package Synchrotron Radiation Workshop in Sirepo, focusing on identifying the ideal slit width and separation for maximizing fringe visibility and intensity. A slit separation of 6 mm and width of 0.5 mm, at a sampling distance of 10.5 m, yielded an estimated energy spread of 1.38×10^{-5} with an associated error of 5.0×10^{-7}. These parameters were implemented in the experimental setup.

The results obtained from both simulation and experimental analysis, conducted using *LabVIEW* and *Python*, were found to be consistent and reliable. This validates the use of SRI as a non-invasive and effective diagnostic tool for high-precision beam characterization in accelerator facilities. Overall, this study demonstrates the feasibility and accuracy of using synchrotron radiation interferometry for beam diagnostics and provides a foundation for future improvements in non-invasive energy spread and emittance measurements.

REFERENCES

[1] CEBAF Nomenclature Document (CND), `https://www.jlab.org/about/cebaf_cnd/overview`

[2] K. Itabashi, T. Akiyama, Y. Fujii, *et al.*, "Study of the nnΛ State and Λn Interaction at Jefferson Lab", Few-Body Syst **63**, 16 (2022). `https://doi.org/10.1007/s00601-021-01717-x`

[3] P. Chevtsov *et al.*, "Non-invasive energy spread monitoring for the JLAB experimental program via synchrotron light interferometers." Nuclear Instruments and Methods in Physics Research Section A: Accelerators, Spectrometers, Detectors and Associated Equipment **557.1** (2006): 324-327.

[4] P.A. Adderley *et al.*, "The Continuous Electron Beam Accelerator Facility at 12 GeV". Phys. Rev. Accel. Beams 27.8, 084802 (2024).

[5] R.P. Walker, "Synchrotron radiation" (1994).

[6] W. Li *et al.*, "Synchrotron Radiation Interferometry for Beam Size Measurement at Low Current and in Large Dynamic Range", Phys. Rev. Accel. Beams **25**, 080702 (2022).

[7] D. Butti, "Synchrotron radiation interferometry for beam size measurement at the Large Hadron Collider", M.S. thesis, Politecnico di Milano, Milan, Italy, 2019.

[8] T. Satogata, Y. Roblin, M.G. Tiefenback, and D.L. Turner, "12 GeV CEBAF Transverse Emittance Evolution", in *Proc. IPAC'15*, Richmond, VA, USA, May 2015, pp. 640–642. `doi:10.18429/JACoW-IPAC2015-WEBD1`

[9] E.D. Courant and H.S. Snyder, "Theory of the Alternating-Gradient Synchrotron", Annals of Physics. **3** (1–2), pp. 360–408, April 2000.

[10] M. Minty and F. Zimmermann, "Measurement and control of charged particle beams." Springer Nature, 2003.

[11] M. Borland, "Features and Applications of the Program ELEGANT", in *Proc. IPAC'13*, Shanghai, China, May 2013, paper THPPA02, pp. 3139–3143.

[12] A.T. Green and Y.-M. Shin, "Implementation of Quadrupole-scan Emittance Measurement at Fermilab's Advanced Superconducting Test Accelerator (ASTA)", in *Proc. IPAC'15*, Richmond, VA, USA, May 2015, pp. 669–671. `doi:10.18429/JACoW-IPAC2015-MOPMA052`

[13] M. Rakitin, *et al.*, "Sirepo: a web-based interface for physical optics simulations-its deployment and use at NSLS-II." Advances in Computational Methods for X-Ray Optics IV. Vol. 10388. SPIE, 2017.

[14] O. Chubar, and R. Celestre. "Memory and CPU efficient computation of the Fresnel free-space propagator in Fourier optics simulations." Optics Express **27**.20 (2019): pp. 28750-28759

[15] C. Elliott *et al.*, "National instruments LabVIEW: a programming environment for laboratory automation and measurement." JALA: Journal of the Association for Laboratory Automation 12.1 (2007): pp. 17–24.

[16] J. Sadowsky, "The continuous wavelet transform: A tool for signal investigation and understanding." Johns Hopkins APL Technical Digest 15 (1994): pp. 306–306

[17] Thorlabs BB2-E02-Ø2 Broadband Dielectric Mirror, 400-750 nm, https://www.thorlabs.com/thorproduct.cfm?partnumber=BB2-E02

[18] Thorlabs FBH473-3 Hard-Coated Bandpass Filter, https://www.thorlabs.com/thorproduct.cfm?partnumber=FBH473-3

[19] Thorlabs LPVISC100 Unmounted Linear Polarizer, 510-800 nm, https://www.thorlabs.com/thorproduct.cfm?partnumber=LPVISC100

[20] Thorlabs LA1779-A-N-BK7 Plano-Convex Lens, 350-700 nm, https://www.thorlabs.com/thorproduct.cfm?partnumber=LA1779-A

[21] Edmund Optics BFS-PGE-120S4M-CS PoE GigE Blackfly®S, Monochrome Camera, https://www.edmundoptics.com/.

[22] Edmund Optics 25.4mm Diameter, Aluminum Coated, Aluminum Substrate Mirror, https://www.edmundoptics.com/p/254mm-dia-aluminum-coated-aluminum-substrate-mirror/7151/

[23] Thorlabs Viewport,Z-L EUV fused Silica (quartz), 2-3 4" UHV, https://www.lesker.com/feedthroughs-viewports.cfm?section=quartz-fused-silica-viewports

Appendix A

IMAGES OF OPTICAL COMPONENTS

This appendix presents images of the optical components used in the synchrotron radiation interferometer described in this thesis. These images gives us good visual clarification of the hardware setup, specifically critical elements such as the broadband dielectric mirror (model BB2-E02, wavelength range 400-750 nm), hard-coated bandpass filter (model FBH473-3), polarizer (model LPVISC100), lens (model LA1779-A), and camera (Blackfly GigE). The inclusion of these images helps to demonstrate the precise alignment, positioning, and integration of optical elements essential for interferometric measurements.

Figure 35. Broadband Dielectric Mirror BB2-E02, 400-750 nm [17].

Figure 36. Hard-Coated Bandpass Filter FBH473-3 [18].

Figure 37. Polarizer LPVISC100 [19].

Figure 38. Lens LA1779-A [20].

Figure 39. Edmund Optics Camera Blackfly GigE [21].

VITA

Sankalp Rajendra Shinde

Department of Physics

Old Dominion University

Norfolk, VA 23529

EDUCATION

2023-2025 (Expected), M.S. Accelerator Physics, Old Dominion University, USA.

2020-2023, B.S. Physics, Fergusson College, India.

PROFESSIONAL EXPERIENCE

2024-2025, Graduate Research Assistant, ODU Research Foundation, Jefferson Lab.

2022-2024, Graduate Teaching Assistant, Old Dominion University.

2022-2023, Project Trainee at Bhabha Atomic Research Center (BARC) Mumbai, India.